SCIENCE IMMUNOLOGY | RESEARCH ARTICLE

CANCER IMMUNOLOGY

A noncanonical cytoplasmic role for BUB1 in restraining DNA damage–induced dsRNA accumulation and sensing within stress granules

Mengjie Hu[1]*, Dong Pan[1], Meng Jiao[1], Xuhui Bao[1], Xinjian Liu[2], Fang Li[1], Chuan-Yuan Li[1,3,4]*

Budding uninhibited by benzimidazoles 1 (BUB1) is a nuclear serine/threonine protein kinase that ensures proper chromosome segregation before mitosis. We report that BUB1 plays an unexpected cytoplasmic role in restraining DNA damage–induced accumulation of cytoplasmic dsRNA and the ensuing immune response. Tumors deficient in BUB1 were sensitive to radiotherapy in a CD8 T cell–dependent manner. We found increased immune cell infiltration accompanied by elevated type I interferon production from irradiated BUB1-deficient cells caused by enhanced cytoplasmic dsRNA accumulation and activation of the MDA5/MAVS dsRNA-sensing pathway. Mechanistically, we found that after radiation exposure, BUB1 underwent nucleus-to-cytoplasm migration, where it bound and phosphorylated the poly(A)-binding protein PABPC1, which was degraded together with its associated messenger RNAs stored in the stress granules, thereby preventing dsRNA accumulation and activation of the innate immune response.

INTRODUCTION

Budding uninhibited by benzimidazoles 1 (BUB1) is a mitotic checkpoint serine/threonine-protein kinase initially identified in genetic screens in the yeast *Saccharomyces cerevisiae* (*1*, *2*). BUB1 binds to the kinetochore and is critical in the mitotic spindle assembly checkpoint (SAC), which ensures accurate chromosome segregation during mitosis (*2*–*5*). Besides its crucial role in regulating the cell cycle, evidence suggests that BUB1 is associated with accelerated Myc-induced lymphoma development in transgenic mice (*6*). Furthermore, the overexpression of BUB1 is implicated in the progression of several human malignancies, including those of the bladder, breast, prostate, and ovary (*7*–*10*). BUB1 is suggested as a prognostic biomarker and therapeutic target for some cancer types (*11*). Bay1816032, a high-affinity BUB1 kinase inhibitor, sensitizes tumor cells toward chemotherapeutic drugs, such as taxanes, ATR (ataxia telengiectasia-related), and poly(ADP-ribose) polymerase inhibitors in vitro and in vivo (*12*). It also sensitizes tumor cells to radiotherapy (*13*). However, the mechanism of BUB1 inhibition–mediated chemotherapy and radiotherapy sensitization has not been elucidated.

Stress granules (SGs) are part of the membrane-less organelles (*14*) that consist of protein-mRNA complexes that form in response to diverse stressors, such as osmotic, oxidative, hypoxic, and mitochondrial stresses, ultraviolet and ionizing radiation, and viral or bacterial infections, in various organisms (from yeast to mammalian cells) (*15*–*17*). SGs contain stalled translating mRNAs, translation initiation components, and additional proteins affecting mRNA function (*18*). They are critical in the antiviral immune response (*19*, *20*) and tumor response to radiotherapy (*21*, *22*). Recent evidence links SG formation to cytosolic viral RNA sensors, such as MDA5 (melanoma differentiation-associated protein 5), RIG-I (retinoic acid-inducible gene I), and double-stranded RNA (dsRNA)–activated protein kinase (*23*), which trigger an innate immune response through type I interferons (IFNs) (*20*). SGs contain nontranslating mRNAs and numerous RNA binding proteins, such as G3BP1 (Ras GTPase-activating protein-binding protein 1), poly(A)-binding protein C1 (PABPC1), TIA1 (TIA1 cytotoxic granule associated RNA binding protein), and Ataxin2 (*17*, *24*, *25*). The poly(A)-binding protein PABPC1 plays a role in regulating mRNA translation and stability (*26*, *27*).

In the present study, we showed that BUB1 deficiency–enhanced tumor radiotherapy was dependent on the DDX58(RIG-I)/MDA5 dsRNA-sensing pathway–induced IFN-stimulated genes (ISGs) and intratumoral lymphocyte infiltration. BUB1 inhibition led to the accumulation of nontranslating dsRNA in the SGs upon ionizing radiation exposure, causing RIG-I/MDA5 activation. In addition, nucleus-localized BUB1 migrated into the cytoplasm to promote proteasome-mediated degradation of PABPC1 and associated mRNA-derived dsRNA, suppressing radiation-induced dsRNA accumulation and type I IFN production. Our findings reveal a cytoplasmic role for BUB1, suggesting potential approaches to enhance radiotherapy and other cytotoxic cancer therapies.

RESULTS

Bub1 in murine tumor radiotherapy and immunotherapy

CRISPR-Cas9 (*28*)–mediated knockdown of Bub1 (fig. S1, A and B) in B16F10 and 4T1 murine tumors did not notably affect growth in vitro (fig. S1, C to G) or in vivo (Fig. 1, A and B). However, radiotherapy efficacy was enhanced substantially in both B16F10-*Bub1KD* (Fig. 1, A and B) and 4T1-*Bub1KD* tumors (Fig. 1, C and D). Because no growth defects were observed in vitro (fig. S1, C to G), we hypothesized that the immune system mediated the enhanced response to radiotherapy in Bub1-deficient tumors. Our results in nude mice (fig. S1, H to J) supported this hypothesis.

Murine glioma CT2A-*Bub1KD* cells (fig. S1K) formed tumors at a slower rate, and radiotherapy completely prevented tumor formation from the *Bub1KO* CT2A cells (Fig. 1, E and F). Radiotherapy "cured" mice showed resistance to WT CT2A rechallenge (Fig. 1, G and H). Furthermore, in Lewis lung carcinoma (LLC) (*29*, *30*), *Bub1KD* strongly enhanced the radiotherapy of LLC (fig. S1, L to N).

---

[1]Department of Dermatology, Duke University School of Medicine, Durham, NC, USA. [2]Department of Biochemistry, School of Medicine, Sun Yat-sen University, Shenzhen, China. [3]Institute for Molecular and Cellular Therapeutics, Chinese Institutes for Medical Research, Beijing, China. [4]School of Basic Medical Sciences, Capital Medical University, Beijing, China.
*Corresponding author. Email: chuan.li@duke.edu (C.-Y.L.); mengjie.hu@duke.edu (M.H.)

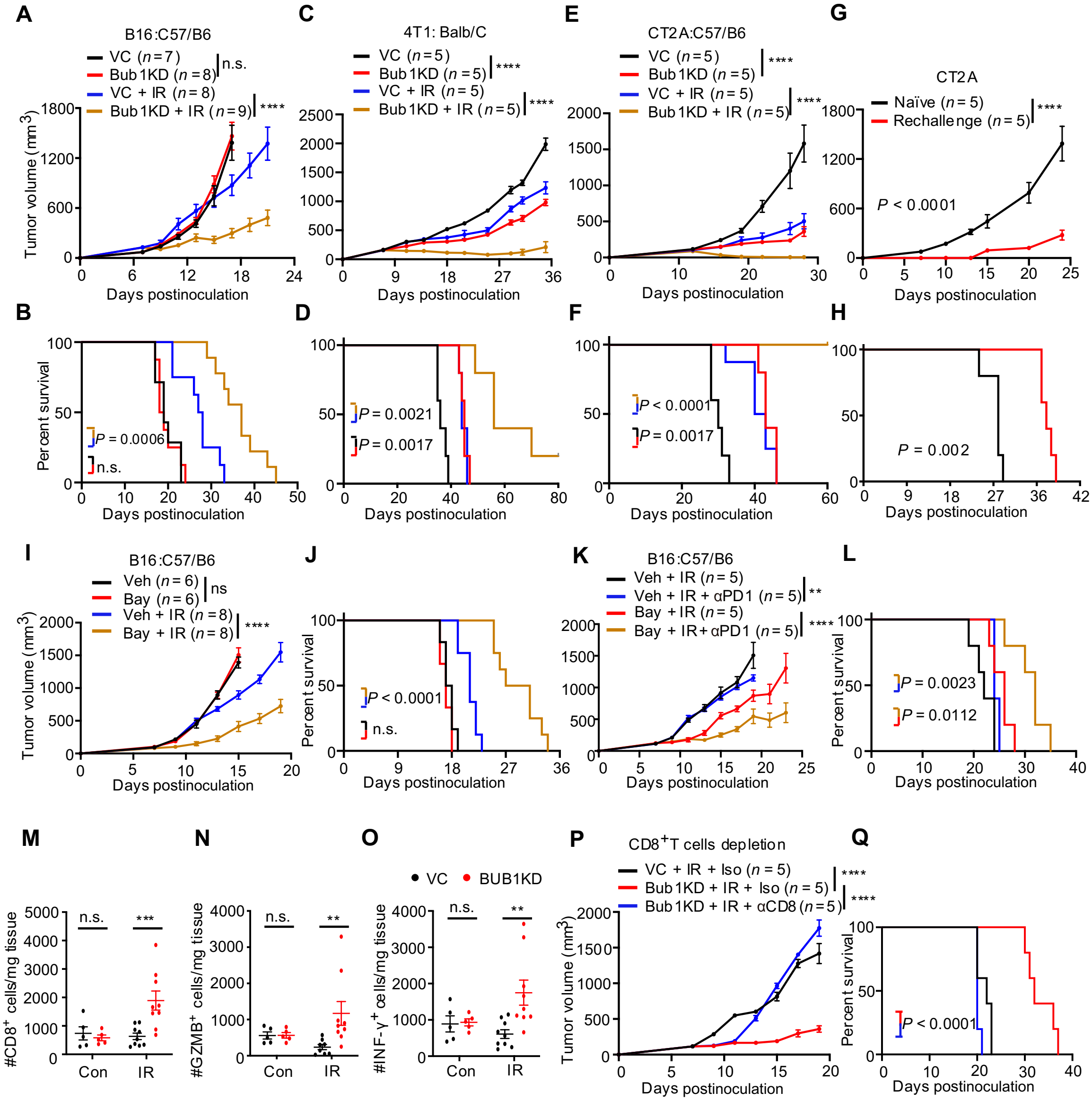

Fig. 1. BUB1 depletion enhances tumor response to radiotherapy and its combination with anti-PD1 therapy. (**A** and **B**) Tumor volume (A) and Kaplan-Meier survival curve (B) of C57BL/6 mice inoculated with about 1 × 10^5 VC or *Bub1KD* B16F10 cells and treated with radiotherapy (8 Gy). (**C** and **D**) Tumor volume (C) and Kaplan-Meier survival curve (D) of Balb/c mice inoculated with about 2 × 10^5 VC or *Bub1KD* 4T1 cells and treated with radiotherapy (8 Gy). (**E** and **F**) Tumor volume (E) and Kaplan-Meier survival curve (F) of C57BL/6 mice inoculated with about 2 × 10^5 VC or *Bub1KD* CT2A cells and treated with radiotherapy (8 Gy). (**G** and **H**) Tumor volume (G) and Kaplan-Meier survival curve (H) of naïve and previously challenged but tumor-free C57BL/6 mice after being inoculated with 1 × 10^5 WT CT2A tumor cells. Tumor-free C57BL/6 mice were rechallenged after remaining tumor-free 60 days after the initial challenge with *Bub1KD* CT2A cells. (**I** and **J**) Tumor volume (I) and Kaplan-Meier survival curve (J) of C57BL/6 mice inoculated with about 1 × 10^5 B16F10 cells and treated with radiotherapy (8 Gy) and Bay1816032 (10 mg/kg) or vehicle (daily from days 4 to 14) postinoculation. (**K** and **L**) Tumor volume (K) and Kaplan-Meier survival curve (L) of C57BL/6 mice inoculated with about 1 × 10^5 B16F10 cells and then treated with radiotherapy (8 Gy), Bub1 inhibitor Bay1816032 (10 mg/kg), or vehicle (daily from days 4 to 14) and treated with 100 μg per mouse anti-PD1 or isotype control antibody on days 11, 14, and 17 postinoculation. (**M** to **O**) Average numbers of tumor-infiltrating CD8 T cells (M), $GZMB^+$ CD8 T cells (N), and IFN-γ^+ CD8 T cells (O) per milligram of tumor tissue from VC or *Bub1KD* B16F10 tumors treated with or without radiotherapy (8 Gy) on day 8 postinoculation. Flow cytometry analysis was done on day 14 after inoculation of 1 × 10^5 tumor cells. Data were grouped from two independent experiments. (**P** and **Q**) Tumor volume (P) and Kaplan-Meier survival curve (Q) of C57BL/6 mice inoculated with about 1 × 10^5 VC or *Bub1KD* B16F10 cells, treated with radiotherapy (8 Gy) and inoculated with 100 μg per mouse of anti-CD8 antibody or isotype control on days 11, 14, and 17. Error bars represent the SEM. *$P < 0.05$; **$P < 0.01$; ***$P < 0.001$; ****$P < 0.0001$; n.s., not significant, as determined by two-way ANOVA [(A), (C), (E), (G), (I), (K), and (M) to (P)] or log-rank test [(B), (D), (F), (H), (J), (L) and (Q)]. Bay, Bay1816032; con, control; IR, ionizing radiation; iso, isotype antibody control; veh, vehicle control.

In further experiments, *Bub1KD* enhanced anti-PD1 (programmed death 1) therapy when combined with radiotherapy in B16F10 tumors (fig. S1, O to Q). Bay1816032, a BUB1 inhibitor, which has been shown to strengthen paclitaxel or docetaxel treatment (*12*), enhanced radiotherapy treatment of B16F10 tumors (fig. S1, R and S, and Fig. 1, I and J). It also enhanced anti-PD1 antibody therapy in combination with radiotherapy (Fig. 1, K and L).

BUB1 in human cancer treatment

BUB1 overexpression was shown to be associated with response to cancer therapies (*31*). We analyzed RNA sequencing (RNA-seq) data of 9736 tumors and 8587 normal tissue samples from TCGA (The Cancer Genome Atlas) using the GEPIA (Gene Expression Profiling Interactive Analysis) website (*32*). We found that expression of *BUB1* was higher in tumor versus normal tissue in 22 of 33 malignancies (fig. S2A). Patients with low *BUB1* expression had a better overall survival (OS) than those with high *BUB1* expression in the TCGA pan-cancer cohort (fig. S2B).

In individual TCGA cohort analysis, we found that in glioblastoma multiforme, bladder cancer, sarcoma, and mesothelioma, radiotherapy-treated patients with low BUB1 mRNA expression (the median value was used to stratify the patients) had better OS than those with high expression. In several other TCGA cohorts, BUB1 mRNA expression levels did not predict clinical outcome (fig. S2, C to M).

In further analysis of RNA-seq data from patients with glioma in the CGGA (Chinese Glioma Genome Atlas) database (*33*), we found that radiation-treated patients with primary glioma with low BUB1 expression had better OS than those with high BUB1 expression (fig. S2N and data file S1). The same applied to patients with CCGA glioma undergoing temozolomide treatment (fig. S2O and data file S1).

BUB1 influences the tumor microenvironment after radiotherapy

We next explored the influences of BUB1 on the human tumor immune microenvironment using the TIP (Tracking Immunophenotype Profiling) tool to analyze the RNA-seq data from radiotherapy- and chemotherapy-treated CGGA glioma with high or low BUB1 expression (*33*, *34*). CIBERSORT analysis showed that CD8 memory T cells were present at higher frequencies in radiotherapy-treated BUB1-low gliomas (fig. S3, A and B). In comparison, the infiltration of B, natural killer (NK), and regulatory T cells showed no significant differences between the two groups (fig. S3, C to E). We subsequently used the gene set enrichment analysis (GSEA) tool to profile anticancer immunity across the seven-step cancer-immunity cycle (fig. S3F) (*35*–*37*). BUB1-low patients had higher overall and individual (steps 3, 4, and 5) immune activity scores than the BUB1-high patients (fig. S3, G to L, and data file S1). Furthermore, the recruitment scores of CD8 T, overall T, T helper 1 (T_H1), T_H2, T_H17, and T_H22 cells were higher in BUB1-low patients. In contrast, monocyte and eosinophil recruitment scores showed no difference (fig. S3, M to T, and data file S1).

We also analyzed the tumor-infiltrating lymphocytes (TILs) in vector control (VC) and Bub1-deficient B16F10 tumors after irradiation (see fig. S4A for flow cytometry gating strategy). Irradiated Bub1-deficient B16F10 tumors had more CD8 and CD4 T cell infiltration than controls (Fig. 1M and fig. S4B). Furthermore, they had increased levels of granzyme-B^+ ($GzmB^+$) CD8 and IFN-γ^+ CD8 T cells (Fig. 1, N and O), indicators of activated cytotoxic T cells. In contrast, radiotherapy caused no significant increases in $NK1.1^+$ NK cells (fig. S4C). In further experiments, we depleted CD8 T cells, CD4 T cells, NK cells, macrophage cells, plasmacytoid dendritic cells, and monocytes and observed their influences on tumor growth. Depletion of CD8 T cells or CD4 T cells abrogated or attenuated radiotherapy-induced tumor growth delay in Bub1-deficient B16F10 tumors. In comparison, depletion of NK cells, macrophage cells, plasmacytoid dendritic cells, and monocytes had no effect (Fig. 1, P and Q, and fig. S4, D to M). Our results suggested that Bub1 deficiency–mediated enhancement of radiotherapy depended on intratumoral infiltration of CD8 and CD4 T cells.

BUB1 inhibition– and radiotherapy-induced type I IFN response

After radiation, GSEA of RNA-seq data of Bub1-deficient B16F10 cells indicated enrichment of the reactome pathways associated with innate immune response and antiviral response compared with VC cells (Fig. 2, A and B, and data file S2). Moreover, the top gene ontology (GO) pathways and biological process (BP) in GO analysis were mainly associated with the cellular immune response to viral infection in Bub1-deficient B16F10 cells (fig. S5, A to D, and data file S2). In the absence of radiation exposure, the top terms of BP in GO pathway analysis were not associated with immune response in Bub1-deficient B16F10 cells (fig. S5E).

Our GSEA highlighted the importance of DDX58(RIG-I)/IFIH1 (inteferon-induced helicase C domain-containing protein 1) pathway (Fig. 2A). Because RIG-I/MDA5 activation synergized with radiotherapy and anti-PD1 therapy (*38*, *39*), we examined this pathway in Bub1KD cells. Bub1 deficiency enhanced radiation-induced transcription of several ISGs downstream of the MDA5 pathway (fig. S5, F to H). Comparable results were observed in B16F10 cells treated with Bay1816032 (fig. S5, I to K). Furthermore, restoration of BUB1 expression in *BUBKD* human HCT116 cells abrogated ISG induction after radiation (fig. S5, L to P).

The IFNAR (interferon-alpha/beta receptor) pathway, directly downstream of interferon regulatory factor 7 (IRF7), was implicated in radiation-induced tumor suppression (*40*). We examined whether IFNAR is involved in Bub1 deficiency–mediated enhancement of radiotherapy. Our results indicated that the blockade of IFNAR attenuated radiation-induced tumor growth delay in Bub1-deficient B16F10 tumors (fig. S5, Q and R).

The MDA5/RIG-I pathway in BUB1 inhibition–mediated radiotherapy enhancement

Protein levels of IRF7, MDA5, and RIG-I increased in irradiated Bub1-deficient B16F10 melanoma (fig. S6A), human breast cancer MDA-MB-231 cells, and human colon cancer HCT116 cells (Fig. 2C and fig. S6, B and C) in a time- and dose-dependent manner when compared with those in VC cells. ISGs are known to be activated by the MDA5 dsRNA-sensing pathway (*41*). To determine whether the MDA5/RIG-I pathway was responsible for Bub1 deficiency–mediated, radiation-induced ISG induction, we generated MDA5–, IRF7–, and RIG-I–knockdown cells in VC and *Bub1KD* cells (fig. S6, D to F). Quantitative reverse transcription polymerase chain reaction (qRT-PCR) analysis of ISG mRNA levels indicated that radiation-induced ISG activation in Bub1-deficient B16F10 cells was attenuated in the double-knockdown (DKD) cells (Fig. 2, D to I, and fig. S6, G to I).

We then compared the tumor formation rates of *Bub1KD*, *Bub1/Mda5-DKD*, *Bub1/Irf7*-DKD, and *Bub1/Rig-I* DKD B16F10 cells in syngeneic C57BL/6 mice undergoing radiotherapy. As expected,

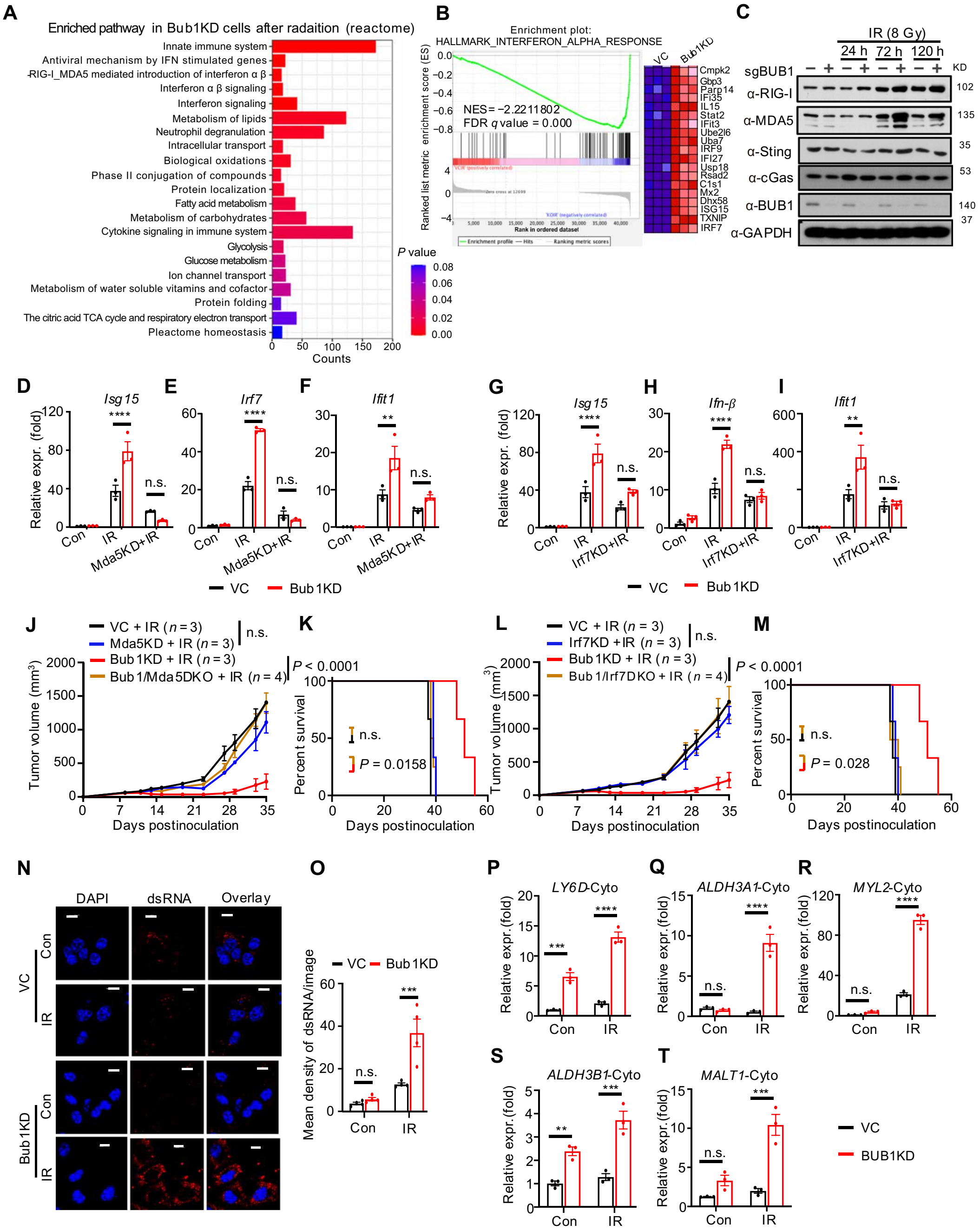

Fig. 2. BUB1 inhibition enables radiation-induced type I IFN induction by promoting cytoplasmic dsRNA accumulation, which activates the RIG-I/MDA5 signaling pathway. (**A**) Reactome analysis of the top 21 up-regulated pathways in *Bub1KD* versus VC B16F10 cells after exposure to 8-Gy x-rays. (**B**) GSEA of IFN-α response in control and *Bub1KD* B16F10 cells treated with radiotherapy (8 Gy). The FDR (false discovery rate) value was calculated using the GSEA tool. NES, normalized enrichment score. (**C**) Protein immunoblot analysis of expression of MDA5, RIG-I, STING (stimulator of interferon genes), and cGas (cyclic GMP-AMP synthase) in VC and BUB1KD MDA-MB-231 cells at 24, 72, and 120 hours after exposure to 8-Gy x-rays. GAPDH was used to control protein loading. (**D** to **F**) Transcription levels of IFN response genes *Isg15* (D), *Irf7* (E), and *Ifit1* (F) in VC, *Bub1KD*, or *Bub1/MDA5DKO* B16F10 cells at 120 hours after exposure to 8-Gy x-rays as analyzed by real-time qRT-PCR. (**G** to **I**) Transcription levels of IFN response genes *ISG15* (G), *IFN*-β (H), and *IFIT1* (I) in VC, *Bub1KD*, or *Bub1/Irf7 DKD* B16F10 cells at 120 hours after exposure to 8-Gy x-rays as analyzed by real-time qRT-PCR. (**J** and **K**) Tumor volume (J) and Kaplan-Meier survival curve (K) of C57BL/6 mice inoculated with about 1×10^5 VC, *Mda5KD*, *Bub1KD*, or *Bub1/Mda5DKD* B16F10 cells and treated with radiotherapy (8 Gy). (**L** and **M**) Tumor volume (L) and Kaplan-Meier survival curve (M) of C57BL/6 mice inoculated with about 1×10^5 VC, *Irf7KD*, *Bub1KD*, or *Bub1/Irf7DKD* B16F10 cells and treated with radiotherapy (8 Gy). (**N** and **O**) Representative immunofluorescence images (N) and relative mean immunofluorescence intensities (O) of dsRNA-specific J2 antibody staining in control and *Bub1KD* B16 after exposure to 8-Gy x-ray. Scale bars, 10 μm. (**P** to **T**) The relative mRNA transcript levels of *Ly6D* (P), *ALDH3A1* (Q), *MYL2* (R), *ALDH3B1* (S), and *MALT1* (T) from the cytoplasmic fractions of control and *BUB1KD* HCT116 cells at 120 hours after exposure to 8-Gy x-rays and by qRT-PCR. Error bars represent the SEM. $*P < 0.05$; $**P < 0.01$; $***P < 0.001$; $****P < 0.0001$; n.s., not significant, as determined by two-way ANOVA [(D) to (F), (G) to (I), (J), (L), and (O) to (T)] or log-rank test [(K) and (M)]. h, hours.

deletion of *Mda5*, *Irf7*, or *Rig-I* (Fig. 2, J to M, and fig. S6J, K) was sufficient to abrogate Bub1 inhibition–elicited antitumor immunity and tumor growth delay upon radiotherapy. In contrast, the ISG transcriptional activation and tumor growth in Bub1-deficient B16F10 cells were not attenuated in *Bub1/Sting*-DKD cells after radiotherapy (fig. S6, L to P). Our results thus suggested that the dsRNA-sensing MDA5/RIG-I pathway was responsible for Bub1 deficiency–mediated tumor growth delay after radiotherapy. Similar results could be found in HCT116 BUB1/MDA5DKO and *BUB1/MAVSDKO* cells (fig. S6, Q to W). In addition, doxorubicin, a commonly used chemotherapy drug (*42*), also induced enhanced expression of MDA5 in the *BUB1KD* HCT116 cells (fig. S6X) when compared with that in VC cells.

BUB1 and radiation-induced cytoplasmic accumulation of dsRNA

The MDA5/RIG-I pathway senses cytoplasmic dsRNA to stimulate an antiviral immune response (*43*). To investigate whether Bub1 inhibition caused enhanced MDA5 pathway activation by inducing cytoplasmic dsRNAs upon radiation or doxorubicin exposure, we used a well-established antibody, J2, to stain dsRNA (*44*). Radiation exposure increased cytoplasmic dsRNA levels in *Bub1KD* B16F10 cells (Fig. 2, N and O) and MDA-MB-231 cells (fig. S7, A and B) compared with those in VC cells. In addition, the BUB1 inhibitor Bay1816032 also induced enhanced cytoplasmic dsRNA accumulation when in combination with radiation (fig. S7, C and D) treatment. In addition, doxorubicin also induced enhanced cytoplasmic dsRNA in the *BUB1KD* HCT116 cells (fig. S7, E and F) compared with that in VC cells.

We conducted RNA-seq analysis to determine the identity of the cytoplasmic RNAs up-regulated in irradiated, BUB1-deficient cells. The top terms of BP and molecular function pathways in GSEA were associated with metabolic process and cytokine production (fig. S7, G to I). We also identified some genes whose mRNAs were up-regulated in *BUB1KD* HCT116 cells treated with irradiation (fig. S7J). We then used qRT-PCR analysis to quantify a subset of the genes. Our analysis indicated that Ly6D (lymphocyte antigen family member D), ALD3A1 (aldehyde dehydrogenase 3A1), ALDH3B1 (aldehyde dehydrogenase 3B1), MYL2 (myosin regulatory light chain 2), and MALT1 (mucosa-associated lymphoid tissue lymphoma translocation protein 1) were increased in BUB1KD cells after radiation (Fig. 2, P to T). To further determine whether some of these radiation–up-regulated cytoplasmic RNAs were in dsRNA forms, we used J2 to pull down the dsRNAs in the lysates and quantified the RNAs by qRT-PCR. We examined 14 J2-bound transcripts and found that they were expressed at higher levels in *BUB1KD* cells after radiation (fig. S8, A to N).

To further prove that the transcripts were in dsRNA form, we used an independent method developed to detect dsRNAs (*45*) and designed two different strand primers (sense and antisense chains) for five different transcripts. We then analyzed the presence of their dsRNA forms through strand-specific RT-PCR (*45*). The result showed that both chains of putative dsRNA forms of each of the five transcripts were up-regulated in the cytoplasm (see fig. S8O for fractionation validation) of BUB1KD HCT116 cells when compared with that in VC cells (fig. S8, P to T).

BUB1 interactions with PABPC1 after radiation exposure

To understand the molecular mechanism of how BUB1 suppressed mRNA-based cytosolic dsRNA accumulation after radiation exposure, we generated HCT116 cells overexpressing Flag-BUB1 (fig. S9A). We then pulled down BUB1 and its associated proteins using an anti-Flag antibody. Liquid chromatography–tandem mass spectrometry (LC-MS/MS) was used to identify interactors of BUB1 in irradiated cells, following established methods (*46*). We identified 67 BUB1-interacting proteins up-regulated and 145 down-regulated after radiation (Fig. 3A, fig. S9B, and data file S3). Among them, PABPC1, a cytoplasmic protein essential for mRNA processing, stability, and protein translation, is ranked as the third most up-regulated BUB1 interactor after radiation. In contrast, the top two BUB1 interactors were BUB1 itself and BUB3, both known to be integral members of the SAC that played prominent roles during mitosis (fig. S9C) (*2*–*5*).

We next used the STRING (Search Tool for the Retrieval of Interacting Genes/Proteins) database, which includes known and predicted protein-protein interactions, to analyze up-regulated and down-regulated proteins among BUB1 interactors after radiation exposure (*47*). GO analysis indicated that among BUB1 interactors, the top up-regulated proteins are mainly involved in RNA processing, whereas the down-regulated proteins are primarily those involved in various cellular metabolic processes (fig. S9D and data file S3). We found many down-regulated proteins among the SG-associated proteins (fig. S9E) (*17*). SGs are protein-RNA complexes that form in response to diverse stressors (such as oxidative stress, ionizing radiation, and infections) in diverse organisms (*15*, *48*). Among them, PABPC1 is considered a major marker of SGs and was previously found to be involved in the formation of SGs (*17*, *49*). Because PABPC1 binds the 3′ end of mRNAs, the interaction of BUB1 with PABPC1 suggested a potential mechanism through which BUB1 could influence RNA levels in the cytoplasm, particularly within the SGs, in irradiated cells.

BUB1 and PABPC1 domains facilitating their interaction

Coimmunoprecipitation (co-IP) assay revealed that HA (hemagglutinin)–PABPC1 interacted with Flag-BUB1 in a radiation-dependent manner (Fig. 3B), and the appearance of upper ladder-like PABPC1 bands hinted at potential ubiquitination of PABPC1 by BUB1, which will be touched on later. The addition of Bay1816032 inhibited radiation-induced interaction between BUB1 and PABPC1 (Fig. 3C), indicating that the interaction depends on BUB1 kinase activity. Next, we attempted to identify the protein domains in BUB1 and PABPC1 responsible for the interaction between the two. BUB1 contains five major domains (Fig. 3D)—TPR (tetratricopeptide), B3BD (Bub3 binding domain), CD1, KEN, and the kinase domain—with the TPR domain critical for Mad3 (MAX dimerization protein 3) binding and the kinase domain responsible for its catalytic function (*50*, *51*). Our co-IP experiment revealed that the only mutant that could not interact with PABPC1 after radiation was the one without the kinase domain (Fig. 3, D and E), thereby suggesting that the kinase domain of *BUB1* was responsible for interacting with PABPC1 after irradiation. This result is consistent with the finding that inhibition of the kinase activity of BUB1 abrogated its radiation-induced interaction with PABPC1 (Fig. 3C).

PABPC1 consists of four RNA binding domains [RRM (RNA recognition motif) 1 to 4], a linker region (PRR; proline-rich region), and a C-terminal MLLE (MademoiseLLE) domain [PABC; poly(A)-binding protein C-terminal domain] (Fig. 3F). RRM1-4 binds poly(A) and can bind adenine/uridine-rich RNA (*26*, *52*), and the C-terminal MLLE domain can facilitate binding to the peptide motif PAM2 (*53*–*55*). The linker region contains serine-proline and threonine-proline residues, and it is critical for translation initiation (*56*). After irradiation, co-IP experiments revealed that the mutant without the

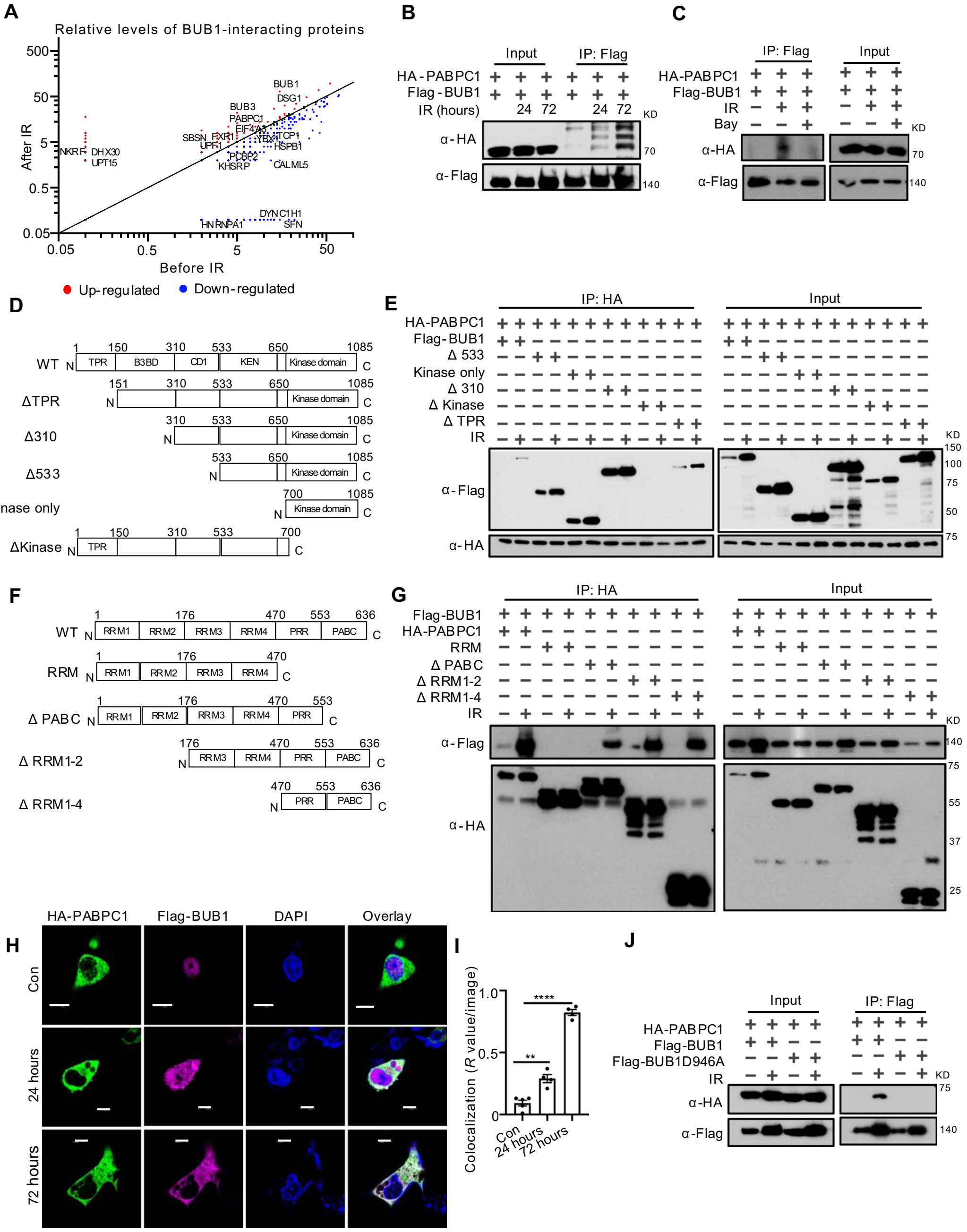

Fig. 3. DNA-damaging stress induces a nucleus-to-cytoplasm migration of BUB1 and its interaction with PABPC1 in the cytoplasm. (**A**) Comparison of individual protein abundance among BUB1-interacting proteins before and after radiation exposure as quantified using LC-MS/MS. Enriched and depleted proteins are indicated using red versus blue dots. (**B**) IP/protein immunoblot analysis of the interaction between Flag-Bub1 and HA-PABPC1 after cellular exposure to x-rays. Plasmids encoding the two genes were transduced into human HCT116 cells, and cells were exposed to 8 Gy of x-rays. Cells were lysed at 24 and 72 hours after x-ray exposure, and the lysates were immunoprecipitated with an anti-Flag antibody. The IP products were then probed with an anti-HA antibody by protein immunoblot analysis. (**C**) IP/protein immunoblot analysis of the interaction between exogenously transduced Flag-Bub1 and HA-PABPC1 in HCT116 cells treated with or without 1 μM Bay1816032 and 72 hours after exposure to 8-Gy x-rays. (**D**) The domain structure of human BUB1 and different truncation mutants used in this study. (**E**) IP/protein immunoblot analysis of the interaction between full-length HA-PABPC1 and full-length or different Flag-BUB1 truncation mutant in the human HCT116 cells. Lysates from cells 72 hours after exposure to 8-Gy x-rays were immunoprecipitated with an anti-HA antibody and probed with an anti-Flag antibody by protein immunoblot analysis. (**F**) The domain structure of human PABPC1 and different truncation mutants generated in this study. (**G**) IP/protein immunoblot analysis of the interaction between full-length Flag-BUB1 and full-length or different HA-PABPC1 truncation mutants in the human HCT116 cells. Lysates were collected from cells 72 hours after exposure to 8-Gy x-rays and were immunoprecipitated with an anti-HA antibody and probed with an anti-Flag antibody by protein immunoblot analysis. (**H** and **I**) Representative immunofluorescence images (H) and quantification of colocalization (I) of Flag-BUB1 and HA-PABPC1 in HCT116 cells at 72 hours after exposure to 8-Gy x-rays. The cells were costained with anti-Flag (magenta) and anti-HA (green) antibodies and DAPI and imaged by confocal microscopy. Scale bars, 10 μm. (**J**) IP/protein immunoblot analysis of the interaction between HA-PABPC1 and WT Flag-BUB1 or a kinase-dead (D946A) version of Flag-BUB1 at 72 hours after exposure to 8-Gy x-rays.

PABC domain could interact with BUB1. At the same time, the one with only the RRM domains could not (Fig. 3, F and G). Together, these results suggested that the proline-rich linker region in PABPC1 was responsible for interacting with BUB1 after irradiation.

Radiation-induced BUB1 migration out of the nucleus

Immunofluorescence staining of Flag-BUB1– and HA-PABPC1–transduced HCT116 cells indicated a nucleus-to-cytoplasm migration of BUB1 by day 3 after radiation exposure. There was a colocalization between BUB1 and PABPC1 in the cytoplasm at 72 hours postirradiation (Fig. 3, H and I), consistent with the co-IP experiments. A BUB1 deletion mutant lacking the kinase domain did not colocalize with PABPC1 (fig. S10, A and B, and data file S4). Meanwhile, a PABPC1 deletion mutant only containing an RRM domain did not colocalize with BUB1 (fig. S10, C and D). To investigate whether the kinase activity was critical for interaction with PABPC1, we constructed a BUB1 kinase–dead mutant (D946A) (*57*) and coexpressed it with HA-PABPC1. As expected, BUB1 kinase–dead mutants could not interact with PABPC1 upon radiation exposure, unlike WT BUB1 (Fig. 3J). Consistently, BUB1 kinase–dead mutant could colocalize with PABPC1 upon radiation exposure, unlike WT BUB1 (fig. S10, E and F). Consistently, cellular exposure to the chemotherapy agent doxorubicin also induced the interaction and colocalization between BUB1 and PABPC1 (fig. S10, G and H, and data file S4). We thus have evidence that BUB1 can migrate from the nucleus to the cytoplasm and that the kinase domain of BUB1 binds to the proline-rich linker region of PABPC1 in the cytoplasm upon cellular exposure to radiation or chemotherapy.

BUB1 regulates dsRNA levels through PABPC1

The canonical role of BUB1 is to function as a member of the SAC, ensuring chromosome integrity during mitosis (*2*–*5*, *58*–*60*). Our results indicated that radiation induced the nucleus-to-cytoplasm migration of BUB1 and its interaction with PABPC1 (Fig. 3). To define the critical domain(s) in BUB1 required to suppress cytoplasmic dsRNA accumulation, we generated BUB1KD HCT116 cells reexpressing various Flag-tagged BUB1 mutants. Radiation induced more dsRNA accumulation in the BUB1KD HCT116 cells compared with that in VC cells, whereas reexpressing BUB1 mutants—including kinase only, ΔTPR, Δ310, and Δ533—inhibited accumulation of dsRNAs after radiation in BUB1KD cells. However, reexpressing Δkinase mutant did not (fig. S11, A and B). Consistently, mRNA levels of ISGs and expression of MDA5, RIG-I, and IRF7 in these cells also showed that reexpression of the BUB1 mutants, including kinase only, ΔTPR, Δ310, and Δ533, inhibited the expression of these genes (fig. S11, C to E). Moreover, reexpressing BUB1 kinase–dead mutant (D946A) did not affect MDA5/RIG-I pathway activity and dsRNA accumulation (fig. S11, F to J) in BUB1KD cells after radiation. Therefore, PABPC1-BUB1 interaction and, specifically, the kinase activity of BUB1 regulate radiation-induced dsRNA accumulation and immune response.

We next demonstrated endogenous nuclear BUB1 translocation to cytoplasm using immunofluorescence staining (Fig. 4, A and B). In addition, using fractionation protein immunoblot analysis, we showed that radiation increased the levels of endogenous BUB1 in the cytoplasm and decreased its expression in the nucleus. Furthermore, Bay1816032 inhibited the radiation-induced cytoplasmic expression of BUB1 and increased the cytoplasmic level of PABPC1 (Fig. 4C and data file S5). Similar results were obtained in BUB1KD B16F10 cells treated with radiation (fig. S12, A to C).

We also showed that PABPC1 strongly colocalized with dsRNA in irradiated *BUB1KD* HCT116 and MDA-MB-231 cells (Fig. 4D and fig. S12, D and E). In addition, using anti-PABPC1–RIP (RNA IP) assay, we showed that radiation increased PABPC1 binding to the dsRNA forms of *ALDH3A1*, *ALDH3B1*, and *LY6D* in *BUB1KD* HCT116 cells when compared with that in VC cells (Fig. 4, E to G). To further investigate whether PABPC1 was responsible for cytoplasmic dsRNA accumulation in BUB1-deficient cells upon radiation, we generated *PABPC1KD* HCT116 cells and treated them with radiation and Bay1816032. Quantitative PCR (qPCR) analysis indicated that *PABPC1* knockdown abrogated radiation-induced elevation of ISG mRNA in the presence of the BUB1 inhibition (fig. S12, F to I). Consistently, it also prevented radiation-induced dsRNA accumulation in the presence of a BUB1 inhibitor (fig. S12, J and K).

To determine whether PABPC1 was functionally responsible for Bub1 deficiency–induced activation of MDA5 pathway and tumor growth suppression after radiotherapy, we generated *Pabpc1KD* and *Bub1/Pabpc1DKD* B16F10 cells (fig. S12L). As expected, depletion of Pabpc1 was sufficient to abrogate Bub1 inhibition–elicited ISG activation and tumor growth delay upon radiotherapy (Fig. 4, H to L).

In further experiments using truncated PABPC1 mutants to demonstrate the importance of BUB1-PABPC1 interaction in suppressing dsRNA accumulation, we showed that the RRM domain–only mutant, which can bind RNA but could not interact with BUB1, could strongly colocalize with radiation-induced dsRNA increase in the presence of a BUB1 inhibitor (fig. S12, M and N). On the other hand, the RRM-deleted mutant HA-ΔRRM1-4, which could not bind RNA, did not colocalize with dsRNA. Furthermore, the ΔPABC mutant, which behaved similarly to WT PABPC1 in co-IP experiments (Fig. 3, F and G), could colocalize with dsRNA. Our results strongly suggest that the BUB1-PABPC1 interaction suppresses cytoplasmic dsRNA accumulation, viral mimicry, and ensuing activation of innate immunity in irradiated cells.

SGs and radiation-induced cytoplasmic dsRNA formation

SGs are ribonucleoprotein assemblies where the bulk of mRNA molecules accumulate. They usually form in response to stress-induced translation inhibition (*15*, *18*, *20*). SGs can form during viral infection and are thought to promote the antiviral response, and many viruses encode inhibitors of SG assembly (*19*, *20*). Moreover, the G3BP1 protein plays an important role during viral infection to prevent excessive innate immune response (*61*, *62*). Our analysis of LC-MS/MS indicated that many SG proteins, especially those associated with RNA processing and metabolism, were associated with BUB1, and the levels of association attenuated markedly after cellular exposure to radiation (fig. S9E). It is well established that SGs contain conserved RNA-protein complexes, including nontranslating mRNAs and RNA binding proteins, such as G3BP1, PABPC1, and TIA1 (*23*, *25*, *49*). We carried out co-IP assay and found that PABPC1 and TIA1 were strongly recruited to G3BP1 SGs in irradiated BUB1-deficient HCT116 cells (Fig. 4M and data file S5), and G3BP1 colocalized with accumulating dsRNA upon radiation treatment in these cells when compared with that in VC cells (Fig. 4, N and O). Because PABPC1 and G3BP1 are core components of SGs (*17*, *49*), our results suggested that BUB1 affects SG protein assembly, especially on dsRNA accumulation within the SGs after stress exposures.

To determine whether SGs are required for activation of the MDA5 pathway, we used ISRIB (integrated stress response inhibitor), a small molecule that prevents the formation of SGs (*63*, *64*), to treat

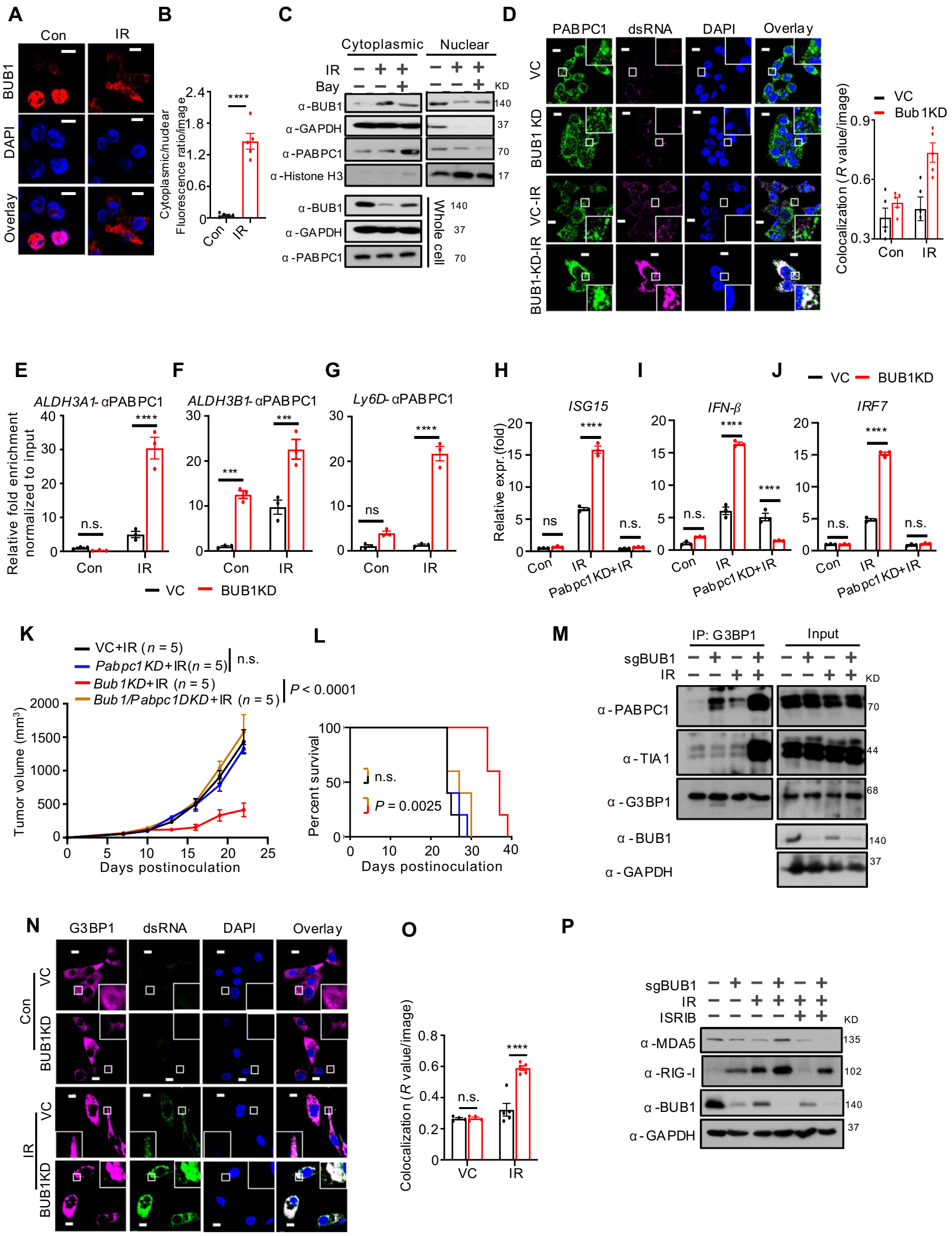

Fig. 4. Cytoplasmic migration of BUB1 and its interaction with PABPC1 is responsible for the suppression of DNA damage–induced cytoplasmic dsRNA accumulation in the SGs and activation of the type I interaction. (**A** and **B**) Representative immunofluorescence images (A) and cytoplasmic/nuclear fluorescence ratio (B) of the endogenous BUB1 protein in HCT116 cells 72 hours after exposure to 8-Gy x-rays. DAPI costaining was conducted to indicate the nucleus. Scale bars, 10 μm. (**C**) Protein immunoblot analysis of expression of BUB1 and PABPC1 in the cytoplasmic fraction, the nuclear fraction, and the whole cell lysates of HCT116 cells treated with or without 1 μM Bay1816032 and 1 μM MG132 for 72 hours after exposure to 8-Gy x-rays. (**D**) Representative immunofluorescence images of PABPC1, dsRNA, and DAPI in VC and BUB1KD HCT116 cells at 120 hours after exposure to 8-Gy x-rays. The cells were costained with anti-PABPC1 (green), anti-dsRNA (magenta), and DAPI. Scale bars, 10 μm. (**E** to **G**) The expression of ALDH3A1 (E), ALDH3B1 (F), and Ly6D (G) in anti-PABPC1 pull-down in control and *BUB1KD* HCT116 cells 120 hours after exposure to 8-Gy x-rays as analyzed by qRT-PCR. (**H** to **J**) Transcription levels of IFN response genes *ISG15* (H), *IFN*-β (I), and *IRF7* (J) in VC, *Bub1KD*, or *Bub1/Pabpc1DKD* B16F10 cells at 120 hours after exposure to 8-Gy x-rays as analyzed by real-time qRT-PCR. (**K** and **L**) Tumor volume (K) and Kaplan-Meier survival curve (L) of C57BL/6 mice inoculated with about 1×10^5 VC, Pabpc1*KD*, *Bub1KD*, or *Bub1/Pabpc1DKD* B16F10 cells and treated with radiotherapy (8 Gy). (**M**) IP/protein immunoblot analysis of the interaction between PABPC1, TIA1, and G3BP1 in VC and BUB1KD HCT116 cells. Lysates were collected from the cells exposed to 8-Gy x-rays for 48 hours and immunoprecipitated with an anti-G3BP1 antibody. The immunoprecipitants were then subjected to protein immunoblot analysis. (**N** and **O**) Representative immunofluorescence costaining image (N) and quantification of colocalization (O) of G3BP1 and dsRNA using an anti-G3BP1 antibody (magenta) and the anti-J2 antibody (green) in VC and BUB1KO HCT116 cells at 120 hours after exposure to 8-Gy x-rays. DAPI was used to indicate the nucleus. Scale bars, 10 μm. (**P**) Protein immunoblot analysis of the expression of MDA5 and RIG-I in VC and BUB1KD HCT116 cells treated with or without 200 nM ISRIB for 72 hours after exposure to 8-Gy x-rays. GAPDH was used as the protein loading control. Error bars represent SEM. $^*P < 0.05$; $^{**}P < 0.01$; $^{***}P < 0.001$; $^{****}P < 0.0001$; n.s., not significant, as determined by unpaired *t* test (B), two-way ANOVA [(E) to (K) and (O)], or log-rank test (L).

irradiated HCT116 cells. Our results showed that ISRB treatment abrogated radiation-induced MDA5 pathway activation in BUB1-deficient HCT116 cells or in Bay1816032-treated cells. In further experiments, we showed that doxorubicin also stimulated the colocalization of G3BP1 and dsRNA in *Bub1KD* B16F10 cells more than VC cells and that Bay1816032 treatment promoted doxorubicin-induced dsRNA accumulation in SGs, as indicated by its colocalization with the well-established SG marker G3BP1 in the cytoplasm. ISRIB treatment inhibited this accumulation (Fig. 4P and fig. S13, A to C). Furthermore, whereas BUB1 deficiency induced dsRNA accumulation within the SGs after radiation, reexpressing BUB1 inhibited the colocalization of dsRNA and G3BP1 (fig. S13, D and E). These data therefore support the finding that BUB1 could restrain dsRNA accumulation within the SGs after radiation.

To determine whether G3BP1 was functionally involved in Bub1 deficiency–induced tumor growth suppression after radiotherapy through increasing the accumulation of dsRNA in the SGs, we compared the tumor formation rates of Bub1KD, G3bp1KD, and *Bub1/G3bp1-DKD* B16F10 cells in syngeneic C57BL/6 mice combined with radiotherapy. As expected, deletion of *G3bp1* (fig. S13, F to H) was sufficient to abrogate Bub1 inhibition–elicited tumor growth delay upon radiotherapy. To further prove that G3BP1 was functionally involved in Bub1 deficiency–mediated, radiation-induced dsRNA accumulation and ISG activation, we generated G3bp1KD B16F10 cells and treated the cells with radiation and a BUB1 inhibitor. Radiation and BUB1 inhibitor treatment–induced expression of MDA5, RIG-I, and IRF7 and ISG activation were abolished in G3bp1KD cells (fig. S13, I to K). In contrast, G3bp2 deficiency enhanced the expression of MDA5 and RIG-I and ISG activation after radiation and Bub1 inhibitor treatment (fig. S13, L to N). These results showed that G3bp1 and G3bp2 are nonredundant in BUB1 deficiency–mediated, radiation-induced MDA5/RIG-I pathway activation.

BUB1 phosphorylation of the PABPC1 linker and cytoplasmic dsRNA levels

Because BUB1's kinase activity appeared critical in regulating PABPC1-associated cytoplasmic dsRNA abundance, we explored whether BUB1 phosphorylated PABPC1 upon irradiation. We first used a pan–anti–phospho-serine/threonine/tyrosine antibody to test PABPC1 phosphorylation status. Our co-IP/protein immunoblot assay indicated that WT (wild-type)–BUB1 could phosphorylate PABPC1 upon radiation exposure, whereas a kinase–dead mutant BUB1KD could not (Fig. 5, A and B, and data file S5). These results thus suggested that PABPC1 was a substrate of BUB1 kinase activity.

To identify the BUB1 phosphorylation site in PABPC1, we used a recently published database that profiled the substrate sequence specificity of 303 serine-threonine kinases (*65*) and predicted potential BUB1 phosphorylation sites within the PABPC1 linker region (fig. S14A). After transducing the mutants into HCT116 cells, our qRT-PCR analysis revealed that radiation exposure induced expression of ISGs in both the STA (S478AT479AS485AT486A-T501A) and the 4A (S478AT479AT501AT582A) mutants (with inactivated potential phosphorylation sites) when compared with WT PABPC1 (Fig 5C and fig. S14, B to D). Moreover, both the STA and 4A mutants elevated the basal levels of ISGs. These results suggested that mutants with nonphosphorylatable sites in the proline-rich linker region were sufficient for stimulating the expression of ISGs. Further experiments showed that the PABPC1 STA mutant could not interact and colocalize with BUB1 upon radiation treatment (Fig. 5C and fig. S14, E and F). In comparison, the PABPC1/STD mutant (mimicking a constitutively phosphorylated PABPC1) not only inhibited radiation induction of MDA5 and IRF7 expression but also attenuated radiation-induced stimulation of ISGs in the presence of Bay1816032 (fig. S14, G to J). In further experiments, we reexpressed PABPC1/STD in HCT116 cells with PABPC1 knockout (PABPC1KD). We then treated the cells with radiation and a BUB1 inhibitor (Bay1816032). BUB1 inhibition induced expression of IRF7 and MDA5 and ISG activation in the VC cells after radiation, which were attenuated in the PABPC1KD cells and the PABPC1KD + STD cells but restored in PABPC1KD + PABPC1 cells (fig. S14, K to M). These results suggested that BUB1-mediated phosphorylation of PABPC1 in the linker region was functionally important after cellular exposure to radiation to suppress dsRNA accumulation and activation of type I IFNs.

BUB1 promotes PABPC1 degradation through phosphorylation-mediated ubiquitination

Given that BUB1 deficiency appeared to increase cytoplasmic PABPC1 levels to boost the amount of dsRNA in the SGs after irradiation, we explored whether BUB1 kinase activity regulated proteasome-mediated degradation of PABPC1. Our earlier results (Fig. 3B) already hinted at the potential ubiquitination of PABPC1 by BUB1. Radiation in combination with *N*-carbobenzyloxy-L-leucyl-L-leucyl-L-leucinal (MG132), a proteosome inhibitor (*66*), induced a typical ubiquitination smear of PABPC1 in the HCT116 cells, which was abrogated in *BUB1KD* HCT116 cells (Fig. 5, D and E). In addition, Bay1816032 also attenuated radiation-induced ubiquitination of PABPC1 (fig. S15A). These results suggested that radiation-induced ubiquitination of PABPC1 depended on the kinase activity of BUB1. Furthermore, we found that a kinase-dead mutant BUB1 inhibited the ubiquitination of PABPC1 and enhanced the cytoplasmic expression of PABPC1 upon radiation treatment when compared with WT BUB1 (Fig. 5F). Furthermore, additional co-IP assays revealed that the STA mutation, which abrogated PABPC1 phosphorylation by BUB1, completely avoided ubiquitination. The 4A mutant, which had a single potential BUB1 phosphorylation site, consistently showed attenuated ubiquitination after radiation (Fig. 5G). These results provided strong evidence that BUB1 phosphorylation of PABPC1 was responsible for mediating radiation-induced ubiquitination of PABPC1. In further support of the importance of BUB1-mediated PABPC1 phosphorylation, our J2/HA-RIP analysis indicated that the addition of a BUB1 kinase inhibitor in combination with radiation treatment enhanced the binding of ALDH3A1, ALDH3B1, and LY6D dsRNA to WT HA-PABPC1, but their binding to PABPC1 (STD) mutant was attenuated or abrogated (fig. S15, B to G).

Using the anti-J2–RIP assay, we showed that the BUB1 inhibitor increased J2 binding to the dsRNA after irradiation in the control cells, which was abolished in PABPC1KD cells. dsRNA levels could not be fully recovered in the PABPC1KD cells reexpressing PABPC1/STD (fig. S15, H to J). Furthermore, we showed that BUB1 deficiency increased J2 binding to the dsRNA after irradiation, which was not attenuated in BUB1KD cells reexpressing BUB1D946A, in contrast with those reexpressing WT BUB1 (fig. S15, K to M).

We next attempted to determine which type of lysine side chain within ubiquitin (Ub) was responsible for the ubiquitination of PABPC1. We generated seven mutant Ub genes, each leaving only one of the seven lysine residues intact. Our co-IP results showed that PABPC1 preferentially interacted with the K27-intact Ub (fig. S15N). This is

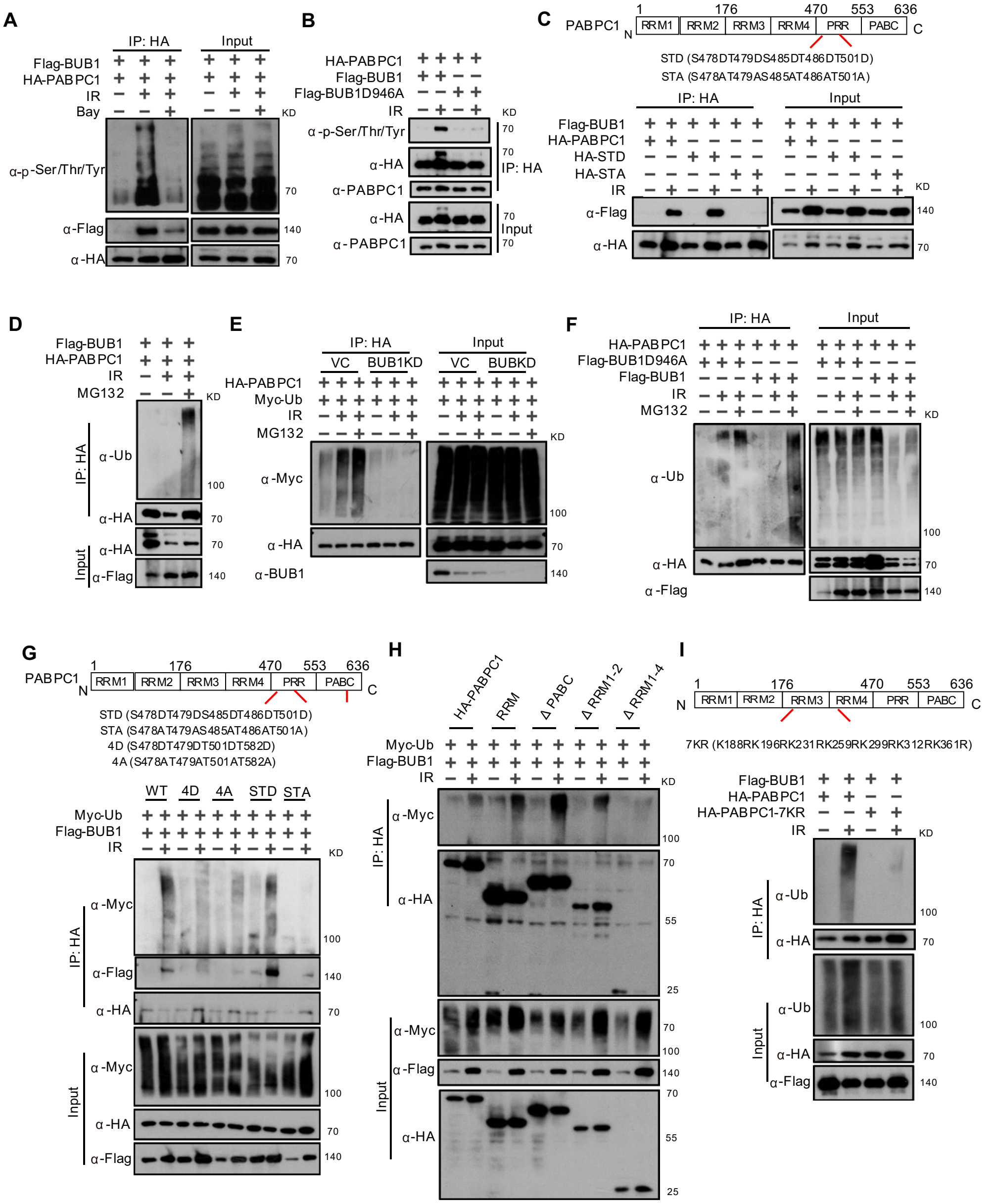

Fig. 5. BUB1 promotes phosphorylation-mediated ubiquitination and degradation of PABPC1 after cellular exposure to DNA damage. (**A**) IP/protein immunoblot analysis of Flag-BUB1 and HA-PABPC1 cotransduced HCT116 cells at 24 and 72 hours after exposure to 8-Gy x-rays. The lysates were immunoprecipitated with an anti-HA antibody and probed with an anti–phospho-serine/threonine/tyrosine antibody to detect potential phosphorylation of PAPBC1. (**B**) IP/protein immunoblot analysis of the Flag-BUB1 or Flag-BUB1D946A (kinase dead) mutant and HA-PABPC1 cotransduced HCT116 cells at 72 hours after exposure to 8 Gy of x-rays. The lysates were immunoprecipitated with an anti-HA antibody and probed with an anti–phospho-serine/threonine/tyrosine antibody by protein immunoblot analysis. (**C**) IP/protein immunoblot analysis of the interaction between Flag-BUB1 and HA-PABPC1, or HA-PABPC1STD, or HA-PABPC1STA mutants at 72 hours after exposure to 8-Gy x-rays. (**D**) IP/protein immunoblot analysis of Flag-BUB1 and HA-PABPC1 cotransduced HCT116 cells at 72 hours after exposure to 8-Gy x-rays and treatment with or without 1 μM MG132. Lysates were immunoprecipitated with an anti-HA antibody and probed with anti-Ub antibody by protein immunoblot analysis. (**E**) IP/protein immunoblot analysis of the Myc-Ub and HA-PABPC1–cotransduced BUB1KD HCT116 and VC cells at 72 hours after exposure to 8-Gy x-rays and treatment with or without 1 μM MG132. Lysates from transduced cells were immunoprecipitated with an anti-HA antibody and probed with anti-Ub antibody by protein immunoblot analysis. (**F**) IP/protein immunoblot analysis of the Flag-BUB1 or Flag-BUB1D946A (kinase dead) and HA-PABPC1–cotransduced HCT116 cells at 72 hours after exposure to 8 Gy of x-rays and treatment with or without 1 μM MG132. The lysates were immunoprecipitated with an anti-HA antibody and probed with anti-Ub antibody on a protein immunoblot. (**G**) IP/protein immunoblot analysis of the Myc-Ub, Flag-BUB1, and WT or phosphorylation mutant HA-PABPC1 cotransduced HCT116 cells at 72 hours after exposure to 8-Gy x-rays. Lysates were immunoprecipitated with an anti-HA antibody and probed with anti-Myc antibody on a protein immunoblot. (**H**) IP/protein immunoblot analysis of the Myc-Ub, Flag-BUB1, and full-length or truncated HA-PABPC1 cotransduced HCT116 cells at 72 hours after exposure to 8-Gy x-rays. Lysates from transduced cells were immunoprecipitated with an anti-HA antibody and probed with anti-Myc antibody by protein immunoblot analysis. (**I**) IP/protein immunoblot analysis of Flag-BUB1 and WT or lysine 7KR mutant HA-PABPC1–cotransduced HCT116 cells at 72 hours after exposure to 8-Gy x-rays. Lysates from transduced cells were immunoprecipitated with an anti-HA antibody and probed with anti-Ub antibody by protein immunoblot analysis.

consistent with early studies that implicated noncanonical K27 poly-Ub as a major player in innate immunity (*67–69*).

We attempted to identify the lysine residue(s) in PABPC1 that were responsible for its ubiquitination. Using different PABPC1 truncation mutants, we showed that RRM, ΔPABC, and ΔRRM1-2 versions of PABPC1 were ubiquitinated upon radiation treatment, but ubiquitination of the ΔRRM1-4 construct mutant of PABPC1 was almost abolished (Fig. 5H). These data suggested that RRM3-4 domains most likely contain the ubiquitination site(s). To narrow down the ubiquitinated site(s) of PABPC1 in the RRM3-4 domain, we used the Rapid UBIquitination (RUBI) detection algorithm (*70*) to predict potential ubiquitination sites within the RRM3-4 domain. RUBI identified seven sites as potentially ubiquitinated. To confirm that these were involved, we generated the PABPC1-7KR mutant, where all seven likely ubiquitinated lysine sites were mutated. As expected, PABPC1 ubiquitination was absent in the 7KR mutant upon radiation treatment, in contrast with WT PABPC1 (Fig. 5I). These data thus established the seven lysine residues within the RRM3-4 domains of PABPC1 as the most likely sites of BUB1-mediated ubiquitination and degradation.

How does PABPC1 regulate mRNA stability in the SGs? Previous studies demonstrate that the interaction between PABPC1 and ERF3 (eukaryotic release factor 3) can help prevent nonsense-mediated mRNA decay (NMD) by physically blocking the recruitment of NMD factors to the termination complex (*71–73*). Consistent with these earlier findings, our data indicated that BUB1 deficiency enhanced PABPC1-bound ERF3, attenuating UPF1 (Up-frameshift suppressor 1) phosphorylation, a key event in NMD activation (fig. S15, O to Q). Therefore, radiation-induced dsRNA stabilization in BUB1-deficient cells appears to involve attenuation of the NMD pathway.

DISCUSSION

In diverse human cancers, high BUB1 expression predicts a worse prognosis. Our data confirmed earlier studies that demonstrate that BUB1 inhibition augments sensitivity to radiotherapy (*13*) and chemotherapy (*12*). We further elucidate BUB1's role in modulating cytosolic dsRNA dynamics, thereby regulating the RIG-I/MDA5–mediated pathway and type I IFN responses after radiotherapeutic and chemotherapeutic interventions. Our finding ascribes a previously undescribed function to BUB1, extending its influence beyond mitotic regulation to encompass critical determinants of cytoplasmic RNA metabolism and innate immune responses under genotoxic stress.

Conceptually, our study supports BUB1 inhibition as an avenue to increase cytotoxic therapy for tumors, using BUB1 inhibitors as potential "immunological radiosensitizers." These agents primarily potentiate the efficacy of intratumoral immune effector cells rather than directly enhancing the cytotoxicity of radiation or chemotherapy to tumor cells. Clinical observations substantiate this mechanism by revealing a correlation between high BUB1 expression and reduced immune cell recruitment and activation posttherapy, correlating with diminished patient survival. Therefore, BUB1 emerges as a promising target to augment the effectiveness of radiotherapy and immunotherapy.

In terms of fundamental BUB1 biology, contrary to its established nuclear role, we show that BUB1 can translocate to the cytoplasm under DNA damage, regulating dsRNA and innate immunity, a function previously unanticipated for an SAC protein. This dual role of BUB1 suggests that it functions as a liaison between cellular stress responses, ensuring a balanced activation of innate immunity, thereby preventing its hyperactivation and potentially harmful effects.

One limitation of our study is that in vivo anti-BUB1 studies were not conducted in human patients or humanized tumor models. Therefore, the relevance of our conclusions to human patients awaits future clinical studies.

In conclusion, our study highlights a critical mechanism where BUB1-mediated phosphorylation leads to PABPC1 ubiquitination and degradation within SGs, mitigating DNA damage–induced dsRNA accumulation and restraining the innate immune response. This revelation expands our understanding of BUB1's repertoire of biological functions and underscores the therapeutic potential of targeting BUB1 to enhance cancer treatment efficacy.

MATERIALS AND METHODS

Study design

This study investigated the role of the mitotic kinase BUB1 in regulating cytoplasmic dsRNA accumulation after DNA damage and the subsequent immune response, using various genetically modified cancer cell lines. To evaluate how BUB1 inhibition affects tumor response to cytotoxic therapy, we treated mice bearing subcutaneous tumors with radiotherapy or chemotherapy combined with immunotherapy. We characterized cytoplasmic dsRNA accumulation and activation of the MDA5/MAVS dsRNA-sensing pathway in irradiated, BUB1-deficient cells using mass spectrometry, flow cytometry, bulk RNA-seq, immunoblotting, and qRT-PCR. Furthermore, we analyzed public databases (TCGA and CGGA) to determine the relationship among BUB1 expression levels, intratumoral lymphocyte infiltration, and survival in radiotherapy-treated patients with cancer. Key experiments were replicated at least twice, with sample sizes, replicates, and statistical methods detailed in the figure legends. Information on materials used in this study, including cell lines and molecular biology agents, is listed in table S1.

Cell culture and x-ray exposure

B16F10 mouse melanoma cells, 4T1 mouse breast carcinoma cells, MDA-MB-231 human breast cancer cells, and HCT116 colon cancer cells were purchased from the Cell Culture Facilities of Duke University School of Medicine. B16F10, HCT116, 4T1, and MDA-MB-231 cells were all grown in Dulbecco's modified Eagle's medium (DMEM) (Sigma-Aldrich) with 10% fetal bovine serum (FBS). All cell lines were periodically subjected to a mycoplasma test using the Universal Mycoplasma Detection Kit (American Type Culture Collection). In some cases, we conducted x-ray irradiation using an X-Rad320 irradiator (Precision; 320 kV and 12.5 mA; part of Duke University School of Medicine Shared Resources) at room temperature. For animal experiments, mice were irradiated on days 8 and/or 11 with 8 gray (Gy) after inoculation of tumor cells into shaved flanks subcutaneously.

Plasmid construction

Human 3×Flag Bub1, HA-PABPC1, and Myc-Ub genes were amplified with Taq 2X Master Mix (M0270L, NEB) using human cDNA made from human embryonic kidney–293 T cells and then cloned into lentivirus-based pLex or pLenti-CMV-Neo (no. 17447, Addgene) vector. Catalytically inactive Bub1 (kinase dead) mutant, truncated Bub1 (ΔTPR, Δ310, Δ533, kinase domain, and Δkinase domain), truncated PABPC1s (RRM, ΔPABC, ΔRRM1-2, and ΔRRM1-4), and phosphorylated site-mutated PABPC1 were constructed using Gibson Assembly Master Mix (E2611, NEB) according to the manufacturer's instructions. Plasmids encoding PABPC1 short hairpin RNAs were purchased from Sigma-Aldrich (26986, NM_002568).

CRISPR-Cas9–mediated gene knockout

Bub1 knockout cells were generated using lentivirus-mediated CRISPR-Cas9 technology. Single-guide RNA (sgRNA) sequences targeting mouse and human Bub1 genes are listed in table S2. Double-stranded oligos encoding the sgRNA sequences were cloned into BsmB1 (Thermo Fisher Scientific)–digested plasmid lentiCRISPRv2 (deposited by F. Zhang of the Massachusetts Institute of Technology to Addgene), which coexpresses Cas9 and sgRNA in the same vector. CRISPR lentivirus vectors were then produced according to an established protocol by the Zhang laboratory. To generate knockout cell lines, target cells were infected with lentivirus, cultured in DMEM (with 10% FBS), and selected in puromycin (1 μg/ml for B16, HCT116, CT2A, LLC, and MDA-MB-231 cells and 2 μg/ml for 4T1 cells). The primers used are listed in table S2.

Tumor growth and treatment in mice

All animal experiments conducted in this study were approved by Duke University Institutional Animal Use and Care Committee (A105-23-24). C57BL/6J and Balb/C mice were purchased from the Jackson Laboratory. Nude mice were purchased from the Division of Laboratory Animal Resources of Duke University. Before tumor cell injection, age-matched 6- to 8-week-old mice were shaved at one of the flanks. Tumor cells were then injected into shaved flanks subcutaneously with lentiCRISPRv2 modified control or target gene-specific knockout tumor cells. Tumor volumes were measured every 2 to 3 days and calculated by the formula (length) × $(\text{width})^2/2$. The mice were sacrificed when tumors reached 2000 mm^3. For x-ray exposure, the tumor-bearing flanks of tumors were irradiated with x-rays using an X-Rad320 irradiator (Precision) with 320 kV and 12.5 mA and with lead shielding to avoid exposure to unintended areas of the mouse's body. For the Bub1 inhibitor treatment, mice were treated orally with vehicle [10% dimethyl sulfoxide (DMSO) and 90% corn oil] and Bay1816032 (10 mg/kg; dissolved in 10% DMSO and 90% corn oil) as indicated in tables and figure legends. For antibody treatments, mice were given 100 μg of antibody via intraperitoneal injection on days 9, 12, and 15 post–tumor cell injection using the following antibodies: anti-PD1 (clone 29F.1A12) or isotype (clone 2A3) from Bio X Cell.

Lymphocyte depletion

To evaluate the role of specific subsets of immune effector cells in mice, we depleted $CD4^+$ T cells, $CD8^+$ T cells, and NK cells with 100 μg of intraperitoneally injected anti-CD4 (GK1.5, Bio X Cell), 100 μg per mouse of anti-CD8b (53-5.8, Bio X Cell), anti-NK1.1 (PK136, Bio X Cell), anti-CD317 (PDCA-1, Bio X Cell), anti-Ly6G/Ly6C (Gr-1, Bio X Cell), and 1 mg per mouse of Standard Macrophage Depletion Kit (Clodrosome + Encapsome, SKU no. CLD-8901, Encapsula NanoSciences), respectively, on days 11, 14, 17 after irradiation on days 8 and 11. Equal amounts of immunoglobulin G (IgG) isotype antibodies (Bio X Cell) were injected as control (table S1).

Analysis of TILs by flow cytometry

About 1×10^5 Bub1 knockout or VC cells were inoculated subcutaneously into C57BL/6J mice. Tumors were excised on day 14 after inoculation (treated with radiation on day 8), weighted, and mechanically minced and incubated in deoxyribonuclease (DNase) I (50 μg/ml; Sigma-Aldrich) and collagenase P (2 mg/ml; Sigma-Aldrich) for 20 min at 37°C. The dissociated cells were passed through a 70-μm cell strainer (BD). The filtered cells were then blocked with an anti-CD16/32 antibody (BioLegend) and stained with indicated surface antibodies for 20 min on ice. Dead cells were excluded using LIVE/DEAD Fixable Aqua dye (Thermo Fisher Scientific). Intracellular antibodies were added after fixation and permeabilization following the manufacturer's instructions (Thermo Fisher Scientific). The anti-mouse fluorochrome-conjugated antibodies are listed in the "Antibodies" and "Reagents and kits" sections in table S1. The stained cells were analyzed using a BD Canto flow cytometry system. The gating strategy for intratumoral lymphocyte analysis is shown in fig. S4A.

In vitro colony formation assay

To compare the clonogenic efficiency of control and *Bub1*KO, B16F10/4T1 cells were seeded in 10-cm plates at 200 cells per plate in triplicate without treatment and 1000 cells per plate in triplicate after exposure to 8-Gy x-ray and allowed to grow for 14 days before staining with crystal violet (dissolved in 20% H_2O and 80% methanol).

Protein immunoblotting

Cell lysates were boiled in SDS sample loading buffer, resolved by 10% SDS–polyacrylamide gel electrophoresis, and transferred to nitrocellulose. The membranes were blocked in 5% milk in tris-buffered saline and Tween 20 [TBST; 10 mM tris-HCl (pH 8.0), 150 mM NaCl, and 0.1% Tween 20] for 1 hour at room temperature. After washing twice with TBST, the membranes were incubated with appropriate primary antibodies in bovine serum albumin/TBST overnight and then washed three times with TBST and probed with horseradish peroxidase–linked anti-Ig (1:5000 dilution) for 1 hour at room temperature. After three washes with TBST, immunoreacted products were visualized using enhanced chemiluminescence reagent and autoradiography.

Immunofluorescence staining

Cells mounted on 35-mm glass-bottom poly-D-lysine–coated dishes were fixed with 4% paraformaldehyde for 20 min after treatment, permeabilized with cold phosphate-buffered saline (PBS) containing 0.1% Triton X-100 for 15 min, blocked with 4% bovine serum in PBS for 1 hour at room temperature, then incubated with primary antibodies (listed in table S1) at room temperature for 3 hours and detected by fluorescein isothiocyanate–labeled anti-IgG (1:400) and Cy3-labeled antibody at room temperature for 1 hour. Cells were costained with 4′,6-diamidino-2-phenylindole (DAPI) to visualize the nuclei. Immunofluorescence images were then obtained using a fluorescence microscope.

Fractionation of nuclear and cytosolic fractions

Vector control and *Bub1KO* cells were treated with Bub1 inhibitor or MG132 on day 3 after exposure to 8-Gy x-ray. The cells were collected and washed using cold PBS, and the cytoplasmic proteins were extracted using NE-PER Nuclear and Cytoplasmic Extraction Reagents (cat. no. 78833, Thermo Fisher Scientific) according to the manufacturer's instructions. In protein immunoblot analysis, we used glyceraldehyde-3-phosphate dehydrogenase (GAPDH) as a loading control for the cytoplasmic fraction and histone H3 for the nuclear fraction.

Co-IP

Cells were harvested in lysis buffer [10 mM tris (pH 7.4), 150 mM NaCl, 1% Triton X-100, and 5 mM EDTA, containing protease inhibitors].

Lysate was incubated with 1 μg of antibody at 4°C for 2 hours. Immunocomplexes were then precipitated with 30 μl of protein A/G Sepharose. After extensive washing with lysis buffer, the beads were boiled in SDS sample loading buffer and assessed by protein immunoblotting (Western blot). HCT116 cells overexpressed with HA-PABPC1, Flag-Bub1, and Myc-Ub were harvested on day 3 after exposure to 8-Gy x-ray and analyzed by co-IP using anti-Myc, anti-HA, or anti-Flag antibody.

RNA extraction

RNA was extracted using the TRIzol Reagent (cat. no. 15596018, Ambion by Life Technologies). Briefly, we rinsed the cells with ice-cold PBS and then added 1 ml of TRIzol to lyse the cells. Next, we scraped the lysate from the petri dish, incubated it at room temperature for 5 min, and added 200 μl of chloroform (cat. no. C2432, Sigma-Aldrich) with vigorous vortexing for 15 s. We then incubated the mixture at room temperature for 10 min and centrifuged it at 12,000*g* for 10 min at 4°C. Next, we transferred the transparent top layer, added 500 μl of isopropanol, and then incubated it at room temperature for 10 min. The mixture was then centrifuged at 12,000*g* for 10 min at 4°C. After removing the supernatant, the pellet was washed with 75% ethanol and centrifuged at 7500*g* for 5 min at 4°C. The RNA was then air-dried and dissolved in 85 μl of ribonuclease (RNase)–free H_2O. Subsequently, we added 5 μl of DNase (cat. no. AM2238, Invitrogen) and 10 μl of 10× TURBO DNase buffer to degrade the remaining DNA at 37°C for 30 min. We then repeated the RNA extraction procedures as described above. Last, we dissolved total RNA free of DNA contamination in RNase-free H_2O and used it for subsequent qPCR and bulk RNA-seq analysis.

RNA sequencing

Total RNAs from VC and *Bub1KO* B16F10 cells on day 3 after exposure to 8-Gy x-rays were prepared as described above, and genome-wide transcriptome analysis was then performed through the Duke Center for Genomic and Computational Biology for sequencing, which quality-checked the samples and prepared cDNA libraries for analysis using Illumina NovaSeq 6000. RNA-seq data were processed using the Trim Galore tool kit, which uses Cutadapt to trim low-quality bases and Illumina sequencing adapters from the 3′ end of the reads. Only reads that were 20 nucleotides or longer after trimming were kept for further analysis. Reads were mapped to the GRCm38.p6 of the mouse genome and transcriptome using the STAR RNA-seq alignment tool. Reads were kept for subsequent analysis if they mapped to a single genomic location using the SAMtools. Gene counts were compiled using the HTSeq tool. Only genes that had at least 10 reads in any given library were used in subsequent analysis. Normalization and differential expression were carried out using the DESeq27 Bioconductor package with the R statistical programming environment. Differentially expressed genes were displayed in heatmaps and volcano plot using the R program (version 3.6.0). GSEA version 10 was used to identify differentially regulated pathways and GO terms for the comparisons were used.

qRT-PCR and qPCR

To quantify RNA expression levels, we used the TRIzol-extracted total RNA (described above) as the template for cDNA synthesis using random hexamer primers (cat. no. SO142, Invitrogen by Thermo Fisher Scientific) and SuperScript II Reverse Transcriptase (cat. no. 18064014, Invitrogen by Thermo Fisher Scientific) following the manufacturer's instructions. Afterward, we performed qRT-PCR of the cDNA using qPCRBIO SyGreen Blue Mix Hi-ROX (cat. no. 17-506C, Genesee Scientific) and the Applied Biosystems ViiA 7 Real-Time PCR System with 384-Well Block (cat. no. 4453536, Thermo Fisher Scientific). We used the comparative Ct (ΔΔCt) method to normalize the expression of individual genes based on β-actin and to compare the relative changes of gene expression among different groups. The primers used are listed in table S3.

LC-MS/MS analysis

To identify BUB1-associated proteins after exposure to x-ray, HCT116 cells infected with Flag-Bub1 or Flag control were collected on day 3 after exposure to x-ray and then were lysed with buffer [10 mM tris (pH 7.4), 150 mM NaCl, 1% Triton X-100, and 5 mM EDTA, containing protease inhibitors]. The lysate was centrifuged at 13,000 rpm for 15 min, and the supernatant was filtered through a 0.22-mm filter (Millipore) followed by the addition of 60 ml of anti-Flag agarose beads (Sigma-Aldrich) and incubation at 4°C for 4 hours with rotations. After IP, the beads were washed two times with buffer II [50 mM Hepes (pH 7.5), 50 mM NaCl, 10 mM EDTA, and 0.1% Triton X-100] and two times with buffer III [50 mM Hepes (pH 7.5), 150 mM NaCl, 10 mM EDTA, and 0.1% Triton X-100]. The immunoprecipitates were then eluted with 75 ml of 33 Flag peptide (20 mg/ml; Sigma-Aldrich) for 1 hour and submitted to the Duke Proteomics Core Facility for trypsin digestion and LC-MS/MS analysis as previously described.

STRING analysis

BUB1-interacting proteins up-regulated or down-regulated, as identified by LC-MS/MS analysis after cellular exposure to radiation, are listed in tables S4 and S5. The STRING website was used to obtain the GO networks associated with the proteins.

RIP qPCR assay

Two 10-cm plates of VC and *BUB1KO* HCT116 cells at 90% confluence were rinsed twice in ice-cold PBS on day 4 after exposure to 8-Gy x-rays, cross-linked at 254 nm (150 mJ/cm^2), collected, and lysed in 1 ml of buffer [10 mM tris (pH 7.4), 150 mM NaCl, 1% Triton X-100, and 5 mM EDTA, containing protease inhibitors] with RNase inhibitor (100 U/ml; Promega N2115). After being kept on ice for 30 min, the cell lysate was centrifuged at 13,000 rpm for 15 min, and the supernatant was collected. One-tenth (volume) of the supernatant was kept as "input" for sample loading quantification, and the rest was subjected to IP. Meanwhile, the anti-HA antibody, anti-J2 antibody, and anti-PABPC1 were conjugated to 50 ml of protein A/G beads and rotated at 4°C for 4 hours, followed by washing three times with RIP buffer [150 mM KCl, 25 mM tris (pH 7.4), 5 mM EDTA, 0.5 mM dithiothreitol, and 0.5% NP-40]. Then, the antibody-conjugated protein A/G beads were incubated with the precleared cell lysate at 4°C overnight. Last, the protein A/G magnetic beads were washed three times with RIP buffer and resuspended in the TRIzol Reagent for RNA extraction. The IP and Input RNA samples were subjected to 1 ml of TRIzol extraction and reverse transcription using the first-strand cDNA synthesis kit (Thermo Fisher Scientific) following the manufacturer's manual. qPCR was then performed using FastStart Universal SYBR Green Master Kit (Roche). The binding of PABPC1 to RNA was then quantified by the ratio of IP RNA normalized to the Input RNA. The primers used are listed in table S3.

Strand-specific RT-PCR

VC and BUB1KD HCT cells were harvested at 120 hours after radiation, and the cytoplasmic proteins were extracted using NE-PER Nuclear and Cytoplasmic Extraction Reagents (cat. no. 78833, Thermo Fisher Scientific) according to the manufacturer's instructions. RNA was extracted from the cytoplasmic part, and both chains (sense and antisense) of dsRNA were quantified through strand-specific RT-PCR (*45*). The primers used are listed in tables S6 and S7.

CIBERSORT analysis of the intratumoral lymphocyte infiltration in human tumors

CIBERSORT is a bioinformatics tool for characterizing the status of anticancer immunity and the proportion of tumor-infiltrating immune cells. We conducted a CIBERSORT analysis of patients with glioma from the CGGA database (www.cgga.org.cn/index.jsp) based on their RNA expression data using an online CIBERTSORT analysis tool, TIP (http://biocc.hrbmu.edu.cn/TIP/), to visualize the immune cell subset of the tumor samples.

Statistical analysis

Quantitative data are presented as means ± SEM, and statistical significance is reported in the figures and/or figure legends. Analysis of variance (ANOVA) with Tukey's post hoc test (one-way ANOVA for comparisons between groups and two-way ANOVA for comparisons of magnitude of changes between different groups) was used to compare values among different experimental groups using the GraphPad PRISM program. For experiments with only two groups, Student's *t* test was used as specified in the figure legends. $P < 0.05$ was considered statistically significant (*), $P < 0.01$ as highly significant (**), $P < 0.001$ (***) and $P < 0.0001$ as extremely significant (****), and n.s. as not significant. Kaplan-Meier estimator and log-rank (Mantel-Cox) tests were used for survival analysis of tumor-bearing mice.

Supplementary Materials

The PDF file includes:

Figs. S1 to S16
Tables S1 to S7
Legends for data files S1 to S5

Other Supplementary Material for this manuscript includes the following:

Data files S1 to S5
MDAR Reproducibility Checklist

REFERENCES AND NOTES

1. F. Pangilinan, Q. Li, T. Weaver, B. C. Lewis, C. V. Dang, F. Spencer, Mammalian BUB1 protein kinases: Map positions and in vivo expression. *Genomics* **46**, 379–388 (1997).
2. D. P. Cahill, C. Lengauer, J. Yu, G. J. Riggins, J. K. Willson, S. D. Markowitz, K. W. Kinzler, B. Vogelstein, Mutations of mitotic checkpoint genes in human cancers. *Nature* **392**, 300–303 (1998).
3. Z. Tang, Y. Sun, S. E. Harley, H. Zou, H. Yu, Human Bub1 protects centromeric sister-chromatid cohesion through Shugoshin during mitosis. *Proc. Natl. Acad. Sci. U.S.A.* **101**, 18012–18017 (2004).
4. S. A. Kawashima, Y. Yamagishi, T. Honda, K. Ishiguro, Y. Watanabe, Phosphorylation of H2A by Bub1 prevents chromosomal instability through localizing shugoshin. *Science* **327**, 172–177 (2010).
5. S. Carvalhal, I. Bader, M. A. Rooimans, A. B. Oostra, J. A. Balk, R. G. Feichtinger, C. Beichler, M. R. Speicher, J. M. van Hagen, Q. Waisfisz, M. van Haelst, M. Bruijn, A. Tavares, J. A. Mayr, R. M. F. Wolthuis, R. A. Oliveira, J. de Lange, Biallelic *BUB1* mutations cause microcephaly, developmental delay, and variable effects on cohesion and chromosome segregation. *Sci. Adv.* **8**, eabk0114 (2022).
6. R. M. Ricke, K. B. Jeganathan, J. M. van Deursen, Bub1 overexpression induces aneuploidy and tumor formation through Aurora B kinase hyperactivation. *J. Cell Biol.* **193**, 1049–1064 (2011).
7. J. Y. Han, Y. K. Han, G. Y. Park, S. D. Kim, C. G. Lee, Bub1 is required for maintaining cancer stem cells in breast cancer cell lines. *Sci. Rep.* **5**, 15993 (2015).
8. C. H. Guo, G. Wu, J. L. Chin, G. Bauman, M. Moussa, F. Wang, N. M. Greenberg, S. S. Taylor, J. W. Xuan, Bub1 up-regulation and hyperphosphorylation promote malignant transformation in SV40 tag-induced transgenic mouse models. *Mol. Cancer Res.* **4**, 957–969 (2006).
9. W. M. Jin, L. M. Ye, KIF4A knockdown suppresses ovarian cancer cell proliferation and induces apoptosis by downregulating BUB1 expression. *Mol. Med. Rep.* **24**, 516 (2021).
10. N. Jiang, Y. Liao, M. Wang, Y. Wang, K. Wang, J. Guo, P. Wu, B. Zhong, T. Guo, C. Wu, BUB1 drives the occurrence and development of bladder cancer by mediating the STAT3 signaling pathway. *J. Exp. Clin. Cancer Res.* **40**, 378 (2021).
11. J. J. Song, C. Ni, X. Dong, C. Sheng, Y. Qu, L. Zhu, *bub1* as a potential oncogene and a prognostic biomarker for neuroblastoma. *Front. Oncol.* **12**, 988415 (2022).
12. G. Siemeister, A. Mengel, A. E. Fernández-Montalván, W. Bone, J. Schröder, S. Zitzmann-Kolbe, H. Briem, S. Prechtl, S. J. Holton, U. Mönning, O. von Ahsen, S. Johanssen, A. Cleve, V. Pütter, M. Hitchcock, F. von Nussbaum, M. Brands, K. Ziegelbauer, D. Mumberg, Inhibition of BUB1 kinase by BAY 1816032 sensitizes tumor cells toward taxanes, ATR, and PARP inhibitors in vitro and in vivo. *Clin. Cancer Res.* **25**, 1404–1414 (2019).
13. A. G. Morales, J. A. Pezuk, M. S. Brassesco, J. C. de Oliveira, R. G. de Paula Queiroz, H. R. Machado, C. G. Carlotti Jr., L. Neder, H. F. de Oliveira, C. A. Scrideli, L. G. Tone, BUB1 and BUBR1 inhibition decreases proliferation and colony formation, and enhances radiation sensitivity in pediatric glioblastoma cells. *Childs Nerv. Syst.* **29**, 2241–2248 (2013).
14. T. Hirose, K. Ninomiya, S. Nakagawa, T. Yamazaki, A guide to membraneless organelles and their various roles in gene regulation. *Nat. Rev. Mol. Cell Biol.* **24**, 288–304 (2023).
15. A. Marcelo, R. Koppenol, L. P. de Almeida, C. A. Matos, C. Nobrega, Stress granules, RNA-binding proteins and polyglutamine diseases: Too much aggregation? *Cell Death Dis.* **12**, 592 (2021).
16. X. Cao, X. Jin, B. Liu, The involvement of stress granules in aging and aging-associated diseases. *Aging Cell* **19**, e13136 (2020).
17. S. Jain, J. R. Wheeler, R. W. Walters, A. Agrawal, A. Barsic, R. Parker, ATPase-modulated stress granules contain a diverse proteome and substructure. *Cell* **164**, 487–498 (2016).
18. A. Khong, T. Matheny, S. Jain, S. F. Mitchell, J. R. Wheeler, R. Parker, The stress granule transcriptome reveals principles of mRNA accumulation in stress granules. *Mol. Cell* **68**, 808–820.e5 (2017).
19. K. Onomoto, M. Yoneyama, G. Fung, H. Kato, T. Fujita, Antiviral innate immunity and stress granule responses. *Trends Immunol.* **35**, 420–428 (2014).
20. C. McCormick, D. A. Khaperskyy, Translation inhibition and stress granules in the antiviral immune response. *Nat. Rev. Immunol.* **17**, 647–660 (2017).
21. B. J. Moeller, Y. Cao, C. Y. Li, M. W. Dewhirst, Radiation activates HIF-1 to regulate vascular radiosensitivity in tumors: Role of reoxygenation, free radicals, and stress granules. *Cancer Cell* **5**, 429–441 (2004).
22. H. Mahboubi, U. Stochaj, Cytoplasmic stress granules: Dynamic modulators of cell signaling and disease. *Biochim. Biophys. Acta Mol. Basis Dis.* **1863**, 884–895 (2017).
23. L. C. Reineke, R. E. Lloyd, The stress granule protein G3BP1 recruits protein kinase R to promote multiple innate immune antiviral responses. *J. Virol.* **89**, 2575–2589 (2015).
24. J. M. Burke, S. L. Moon, T. Matheny, R. Parker, RNase L reprograms translation by widespread mRNA turnover escaped by antiviral mRNAs. *Mol. Cell* **75**, 1203–1217 e1205 (2019).
25. L. A. Becker, B. Huang, G. Bieri, R. Ma, D. A. Knowles, P. Jafar-Nejad, J. Messing, H. J. Kim, A. Soriano, G. Auburger, S. M. Pulst, J. P. Taylor, F. Rigo, A. D. Gitler, Therapeutic reduction of ataxin-2 extends lifespan and reduces pathology in TDP-43 mice. *Nature* **544**, 367–371 (2017).
26. Y. Qi, M. Wang, Q. Jiang, PABPC1—mRNA stability, protein translation and tumorigenesis. *Front. Oncol.* **12**, 1025291 (2022).
27. M. Wydro, A. Bobrowicz, R. J. Temperley, R. N. Lightowlers, Z. M. Chrzanowska-Lightowlers, Targeting of the cytosolic poly(A) binding protein PABPC1 to mitochondria causes mitochondrial translation inhibition. *Nucleic Acids Res.* **38**, 3732–3742 (2010).
28. L. Cong, F. A. Ran, D. Cox, S. Lin, R. Barretto, N. Habib, P. D. Hsu, X. Wu, W. Jiang, L. A. Marraffini, F. Zhang, Multiplex genome engineering using CRISPR/Cas systems. *Science* **339**, 819–823 (2013).
29. V. Olivo Pimentel, D. Marcus, A. M. van der Wiel, N. G. Lieuwes, R. Biemans, R. I. Lieverse, D. Neri, J. Theys, A. Yaromina, L. J. Dubois, P. Lambin, Releasing the brakes of tumor immunity with anti-PD-L1 and pushing its accelerator with L19-IL2 cures poorly immunogenic tumors when combined with radiotherapy. *J. Immunother. Cancer* **9**, e001764 (2021).
30. A. A. Mathew, Z. T. Zakkariya, A. Ashokan, M. Manohar, P. Keechilat, S. V. Nair, M. Koyakutty, 5-FU mediated depletion of myeloid suppressor cells enhances T-cell infiltration and anti-tumor response in immunotherapy-resistant lung tumor. *Int. Immunopharmacol.* **120**, 110129 (2023).
31. Y. Cicirò, D. Ragusa, A. Sala, Expression of the checkpoint kinase BUB1 is a predictor of response to cancer therapies. *Sci. Rep.* **14**, 4461 (2024).
32. Z. Tang, C. Li, B. Kang, G. Gao, C. Li, Z. Zhang, GEPIA: A web server for cancer and normal gene expression profiling and interactive analyses. *Nucleic Acids Res.* **45**, W98–W102 (2017).

33. Z. Zhao, K.-N. Zhang, Q. Wang, G. Li, F. Zeng, Y. Zhang, F. Wu, R. Chai, Z. Wang, C. Zhang, W. Zhang, Z. Bao, T. Jiang, Chinese Glioma Genome Atlas (CGGA): A comprehensive resource with functional genomic data from chinese glioma patients. *Genomics Proteomics Bioinformatics* **19**, 1–12 (2021).
34. L. Xu, C. Deng, B. Pang, X. Zhang, W. Liu, G. Liao, H. Yuan, P. Cheng, F. Li, Z. Long, M. Yan, T. Zhao, Y. Xiao, X. Li, TIP: A web server for resolving tumor immunophenotype profiling. *Cancer Res.* **78**, 6575–6580 (2018).
35. I. Mellman, D. S. Chen, T. Powles, S. J. Turley, The cancer-immunity cycle: Indication, genotype, and immunotype. *Immunity* **56**, 2188–2205 (2023).
36. A. M. Newman, C. B. Steen, C. L. Liu, A. J. Gentles, A. A. Chaudhuri, F. Scherer, M. S. Khodadoust, M. S. Esfahani, B. A. Luca, D. Steiner, M. Diehn, A. A. Alizadeh, Determining cell type abundance and expression from bulk tissues with digital cytometry. *Nat. Biotechnol.* **37**, 773–782 (2019).
37. A. M. Newman, C. L. Liu, M. R. Green, A. J. Gentles, W. Feng, Y. Xu, C. D. Hoang, M. Diehn, A. A. Alizadeh, Robust enumeration of cell subsets from tissue expression profiles. *Nat. Methods* **12**, 453–457 (2015).
38. D. Pan, X. Bao, M. Hu, M. Jiao, F. Li, C.-Y. Li, SETDB1 restrains endogenous retrovirus expression and antitumor immunity during radiotherapy. *Cancer Res.* **82**, 2748–2760 (2022).
39. W. X. Zheng, D. R. E. Ranoa, X. Huang, Y. Hou, K. Yang, E. C. Poli, M. A. Beckett, Y.-X. Fu, R. R. Weichselbaum, RIG-I–like receptor LGP2 is required for tumor control by radiotherapy. *Cancer Res.* **80**, 5633–5641 (2020).
40. B. C. Burnette, H. Liang, Y. Lee, L. Chlewicki, N. N. Khodarev, R. R. Weichselbaum, Y.-X. Fu, S. L. Auh, The efficacy of radiotherapy relies upon induction of type I interferon-dependent innate and adaptive immunity. *Cancer Res.* **71**, 2488–2496 (2011).
41. T. Kawai, K. Takahashi, S. Sato, C. Coban, H. Kumar, H. Kato, K. J. Ishii, O. Takeuchi, S. Akira, IPS-1, an adaptor triggering RIG-I- and Mda5-mediated type I interferon induction. *Nat. Immunol.* **6**, 981–988 (2005).
42. C. Carvalho, R. X. Santos, S. Cardoso, S. Correia, P. J. Oliveira, M. S. Santos, P. I. Moreira, Doxorubicin: The good, the bad and the ugly effect. *Curr. Med. Chem.* **16**, 3267–3285 (2009).
43. A. G. D. Junior, N. G. Sampaio, J. Rehwinkel, A balancing act: MDA5 in antiviral immunity and autoinflammation. *Trends Microbiol.* **27**, 75–85 (2019).
44. K. N. Son, Z. G. Liang, H. L. Lipton, Double-stranded RNA is detected by immunofluorescence analysis in RNA and DNA virus infections, including those by negative-stranded RNA viruses. *J. Virol.* **89**, 9383–9392 (2015).
45. S. Kim, J. Yoon, K. Lee, Y. Kim, Analysis of mitochondrial double-stranded RNAs in human cells. *STAR Protoc.* **4**, 102007 (2023).
46. W. Bian, H. Jiang, S. Feng, J. Chen, W. Wang, X. Li, Protocol for establishing a protein-protein interaction network using tandem affinity purification followed by mass spectrometry in mammalian cells. *STAR Protoc.* **3**, 101569 (2022).
47. P. Bernard, K. Hardwick, J. P. Javerzat, Fission yeast bub1 is a mitotic centromere protein essential for the spindle checkpoint and the preservation of correct ploidy through mitosis. *J. Cell Biol.* **143**, 1775–1787 (1998).
48. C. L. Riggs, N. Kedersha, P. Ivanov, P. Anderson, Mammalian stress granules and P bodies at a glance. *J. Cell Sci.* **133**, jcs242487 (2020).
49. A. Aulas, M. M. Fay, S. M. Lyons, C. A. Achorn, N. Kedersha, P. Anderson, P. Ivanov, Stress-specific differences in assembly and composition of stress granules and related foci. *J. Cell Sci.* **130**, 927–937 (2017).
50. K. Overlack, I. Primorac, M. Vleugel, V. Krenn, S. Maffini, I. Hoffmann, G. J. P. L. Kops, A. Musacchio, A molecular basis for the differential roles of Bub1 and BubR1 in the spindle assembly checkpoint. *eLife* **4**, e05269 (2015).
51. I. Leontiou, N. London, K. M. May, Y. Ma, L. Grzesiak, B. Medina-Pritchard, P. Amin, A. A. Jeyaprakash, S. Biggins, K. G. Hardwick, The Bub1-TPR domain interacts directly with Mad3 to generate robust spindle checkpoint arrest. *Curr. Biol.* **29**, 2407–2414.e7 (2019).
52. G. Kozlov, J. F. Trempe, K. Khaleghpour, A. Kahvejian, I. Ekiel, K. Gehring, Structure and function of the C-terminal PABC domain of human poly(A)-binding protein. *Proc. Natl. Acad. Sci. U.S.A.* **98**, 4409–4413 (2001).
53. A. Ivanov, E. Shuvalova, T. Egorova, A. Shuvalov, E. Sokolova, N. Bizyaev, I. Shatsky, I. Terenin, E. Alkalaeva, Polyadenylate-binding protein-interacting proteins PAIP1 and PAIP2 affect translation termination. *J. Biol. Chem.* **294**, 8630–8639 (2019).
54. E. Huntzinger, J. E. Braun, S. Heimstadt, L. Zekri, E. Izaurralde, Two PABPC1-binding sites in GW182 proteins promote miRNA-mediated gene silencing. *EMBO J.* **29**, 4146–4160 (2010).
55. A. Hildebrandt, A. Hildebrandt, M. Brüggemann, C. Rücklé, S. Boerner, J. B. Heidelberger, A. Busch, H. Hänel, A. Voigt, M. M. Möckel, S. Ebersberger, A. Scholz, A. Dold, T. Schmid, I. Ebersberger, J.-Y. Roignant, K. Zarnack, J. König, P. Beli, The RNA-binding ubiquitin ligase MKRN1 functions in ribosome-associated quality control of poly(A) translation. *Genome Biol.* **20**, 216 (2019).
56. O. P. de Melo Neto, T. D. C. da Costa Lima, K. C. Merlo, T. P. Romão, P. O. Rocha, L. A. Assis, L. M. Nascimento, C. C. Xavier, A. M. Rezende, C. R. S. Reis, B. Papadopoulou, Phosphorylation and interactions associated with the control of the *Leishmania* poly-A binding protein 1 (PABP1) function during translation initiation. *RNA Biol.* **15**, 739–755 (2018).
57. A. Asghar, A. Lajeunesse, K. Dulla, G. Combes, P. Thebault, E. A. Nigg, S. Elowe, Bub1 autophosphorylation feeds back to regulate kinetochore docking and promote localized substrate phosphorylation. *Nat. Commun.* **6**, 8364 (2015).
58. T. Kim, A. Gartner, Bub1 kinase in the regulation of mitosis. *Anim. Cells Syst.* **25**, 1–10 (2021).
59. V. M. Bolanos-Garcia, T. L. Blundell, BUB1 and BUBR1: Multifaceted kinases of the cell cycle. *Trends Biochem. Sci.* **36**, 141–150 (2011).
60. S. S. Taylor, F. McKeon, Kinetochore localization of murine Bub1 is required for normal mitotic timing and checkpoint response to spindle damage. *Cell* **89**, 727–735 (1997).
61. M. Paget, C. Cadena, S. Ahmad, H.-T. Wang, T. X. Jordan, E. Kim, B. Koo, S. M. Lyons, P. Ivanov, B. tenOever, X. Mu, S. Hur, Stress granules are shock absorbers that prevent excessive innate immune responses to dsRNA. *Mol. Cell* **83**, 1180–1196.e8 (2023).
62. J. M. Burke, O. C. Ratnayake, J. M. Watkins, R. Perera, R. Parker, G3BP1-dependent condensation of translationally inactive viral RNAs antagonizes infection. *Sci. Adv.* **10**, eadk8152 (2024).
63. C. Sidrauski, A. M. McGeachy, N. T. Ingolia, P. Walter, The small molecule ISRIB reverses the effects of eIF2α phosphorylation on translation and stress granule assembly. *eLife* **4**, e05033 (2015).
64. H. H. Rabouw, M. A. Langereis, A. A. Anand, L. J. Visser, R. J. de Groot, P. Walter, F. J. M. van Kuppeveld, Small molecule ISRIB suppresses the integrated stress response within a defined window of activation. *Proc. Natl. Acad. Sci. U.S.A.* **116**, 2097–2102 (2019).
65. J. L. Johnson, T. M. Yaron, E. M. Huntsman, A. Kerelsky, J. Song, A. Regev, T. Y. Lin, K. Liberatore, D. M. Cizin, B. M. Cohen, N. Vasan, Y. Ma, K. Krismer, J. T. Robles, B. van de Kooij, A. van Vlimmeren, N. Andrée-Busch, N. F. Käufer, M. V. Dorovkov, A. G. Ryazanov, Y. Takagi, E. R. Kastenhuber, M. D. Goncalves, B. D. Hopkins, O. Elemento, D. J. Taatjes, A. Maucuer, A. Yamashita, A. Degterev, M. Uduman, J. Lu, S. D. Landry, B. Zhang, I. Cossentino, R. Linding, J. Blenis, P. V. Hornbeck, B. E. Turk, M. B. Yaffe, L. C. Cantley, An atlas of substrate specificities for the human serine/threonine kinome. *Nature* **613**, 759–766 (2023).
66. L. Zhang, H. Tang, Y. Kou, R. Li, Y. Zheng, Q. Wang, X. Zhou, L. Jin, MG132-mediated inhibition of the ubiquitin-proteasome pathway ameliorates cancer cachexia. *J. Cancer Res. Clin. Oncol.* **139**, 1105–1115 (2013).
67. M. Tracz, W. Bialek, Beyond K48 and K63: Non-canonical protein ubiquitination. *Cell. Mol. Biol. Lett.* **26**, 1 (2021).
68. M. van Huizen, M. Kikkert, The role of atypical ubiquitin chains in the regulation of the antiviral innate immune response. *Front. Cell Dev. Biol.* **7**, 392 (2019).
69. Q. Zhou, J. Zhang, K27-linked noncanonic ubiquitination in immune regulation. *J. Leukoc. Biol.* **111**, 223–235 (2022).
70. I. Walsh, T. Di Domenico, S. C. Tosatto, RUBI: Rapid proteomic-scale prediction of lysine ubiquitination and factors influencing predictor performance. *Amino Acids* **46**, 853–862 (2014).
71. A. Kishor, S. E. Fritz, J. R. Hogg, Nonsense-mediated mRNA decay: The challenge of telling right from wrong in a complex transcriptome. *Wiley Interdiscip. Rev. RNA* **10**, e1548 (2019).
72. P. V. Ivanov, N. H. Gehring, J. B. Kunz, M. W. Hentze, A. E. Kulozik, Interactions between UPF1, eRFs, PABP and the exon junction complex suggest an integrated model for mammalian NMD pathways. *EMBO J.* **27**, 736–747 (2008).
73. I. Peixeiro, Â. Inácio, C. Barbosa, A. L. Silva, S. A. Liebhaber, L. Romão, Interaction of PABPC1 with the translation initiation complex is critical to the NMD resistance of AUG-proximal nonsense mutations. *Nucleic Acids Res.* **40**, 1160–1173 (2012).

Acknowledgments: We thank the Flow Cytometry Facility of Duke University School of Medicine for assistance. We also thank the Duke University Light Microscopy Core Facility for professional help using confocal microscopy. **Funding:** This study was funded in part by National Institutes of Health grant CA251439 (C.-Y.L.), National Institutes of Health grant CA272591 (C.-Y.L.), and Lung Cancer Initiative grant (C.-Y.L.). **Author contributions:** Conceptualization: M.H. and C.-Y.L. Methodology: M.H., M.J., D.P., X.B., X.L., and F.L. Investigation: M.H, M.J, D.P., X.B., and X.L. Funding acquisition: C.-Y.L. and F.L. Project administration: C.-Y.L., F.L., and M.H. Supervision: C.-Y.L. and F.L. Writing—original draft: M.H. and C.-Y.L. Writing—review and editing: M.H., C.-Y.L., and F.L. **Competing interests:** The authors declare that they have no competing interests. **Data and materials availability:** All data needed to evaluate the conclusions in the paper are present in the paper or the Supplementary Materials, with the exception of RNA-seq data, which are deposited in the GEO database (GEO246123 and GEO2461124). The raw experimental data used to generate figures, including protein immunoblots, are provided in separate data file tables (data files S1 to S5). Plasmids and cell lines generated in the study are available upon request to the first or corresponding authors.

Submitted 2 May 2024
Resubmitted 19 March 2025
Accepted 16 July 2025
Published 8 August 2025
10.1126/sciimmunol.adq2055